

## STAR CLUSTER POPULATIONS IN THE OUTER DISKS OF NEARBY GALAXIES

STÉPHANE HERBERT-FORT<sup>1</sup>, DENNIS ZARITSKY<sup>1</sup>, JOHN MOUSTAKAS<sup>2</sup>,  
ANDREA DI PAOLA<sup>3</sup>, RICHARD W. POGGE<sup>4</sup>, ROBERTO RAGAZZONI<sup>5</sup>

<sup>1</sup>University of Arizona/Steward Observatory, 933 N Cherry Avenue, Tucson, AZ 85721 USA  
(email: s.herbertfort@gmail.com, dennis.zaritsky@gmail.com)

<sup>2</sup>Center for Astrophysics and Space Sciences, University of California, San Diego, La Jolla, CA 92093, USA

<sup>3</sup>INAF, Osservatorio Astronomico di Roma, via di Frascati 33, I-00040 Monteporzio, Italy

<sup>4</sup>Department of Astronomy, The Ohio State University, 140 W. 18th Avenue, Columbus, OH 43210-1173

<sup>5</sup>INAF, Osservatorio Astronomico di Padova, vicolo dell'Osservatorio 5, I-35122 Padova, Italy

*Draft version August 21, 2021*

### ABSTRACT

We present a Large Binocular Telescope (LBT) imaging study that characterizes the star cluster component of nearby galaxy outer disks (beyond the optical radius  $R_{25}$ ). Expanding on the pilot project of Herbert-Fort et al. (2009), we present deep ( $\sim 27.5$  mag  $V$ -band point-source limiting magnitude)  $U$ - and  $V$ -band imaging of six galaxies: IC 4182, NGC 3351, NGC 4736, NGC 4826, NGC 5474, and NGC 6503. We find that the outer disk of each galaxy is populated with marginally-resolved star clusters with masses  $\sim 10^3 M_{\odot}$  and ages up to  $\sim 1$  Gyr (masses and ages are limited by the depth of our imaging and uncertainties are large given how photometry can be strongly affected by the presence or absence of a few stars in such low mass systems), and that they are typically found out to at least  $2R_{25}$  but sometimes as far as 3 to 4  $R_{25}$  – even beyond the apparent H I disk. The mean rate of cluster formation for  $1R_{25} \leq R \leq 1.5R_{25}$  is at least one every  $\sim 2.5$  Myr and the clusters are spatially correlated with the H I, most strongly with higher density gas near the periphery of the optical disk and with lower density neutral gas at the H I disk periphery. We hypothesize that the clusters near the edge of the optical disk are formed in the extension of spiral structure from the inner disk and are a fairly consistent phenomenon and that the clusters formed at the periphery of the H I disk are the result of accretion episodes.

*Subject headings:* galaxies: star clusters – galaxies: structure – methods: statistical – facility:LBT

### 1. INTRODUCTION

In the current paradigm of galaxy evolution, material continually accretes onto galaxies. As such, the outer extremities are particularly interesting environments, but they are notoriously difficult to study. The surface brightness of the diffuse stellar component drops well below the background sky level (Pohlen et al. 2002), the neutral gas becomes ionized (Maloney 1993), and observing the diffuse ionized gas requires long exposures on the largest telescopes while still being limited to within the radial extent of the neutral gas (Christlein & Zaritsky 2008).

The GALEX mission (Martin et al. 2005) highlighted an alternative approach to the study of outer disks by clearly identifying large populations of apparent young stellar clusters in the outskirts of some nearby disk galaxies (Thilker et al. 2005; Gil de Paz et al. 2005; Zaritsky & Christlein 2007). GALEX UV imaging proved particularly useful in this regard because it provides the stark color contrast required to easily differentiate young, blue clusters from the sea of redder background objects. Of course, any method that distinguishes between young clusters and background objects can be used to the same effect, and so, narrowband H $\alpha$  imaging both predates the GALEX work (Ferguson et al. 1998) and still provides new results (Werk et al. 2010). While having certain advantages, the drawback of the H $\alpha$  work, and to a lesser extent the GALEX studies, is that they focus on the youngest clusters, which limits the number of such objects available for study and also our ability to measure the long-term history of this galactic component. Nevertheless, the value of these studies is evidenced by the increase in corresponding theoret-

ical studies (e.g. Bush et al. 2008; Roškar et al. 2008a,b; Kazantzidis et al. 2009).

As useful as GALEX has been for detecting large populations of outer disk clusters, this paper focuses instead on broadband optical imaging of outer disks for several reasons. First, the spatial resolution of GALEX imaging ( $\sim 5''$  FWHM) is roughly six times poorer than what we normally achieve using ground-based optical telescopes. Therefore, the candidate clusters identified by GALEX are typically blends of multiple clusters (Gil de Paz et al. 2005), as can also be seen in the comparison we provide in Figure 1. Until we establish what the typical mass of our detected objects is, we will refer to these objects as stellar knots, which is a purely observational definition of an individual object identified in the available images, to avoid prejudging their true physical nature. Of course, even after we have an estimate of the typical mass one must remain aware that any particular detection may be quite different from the mean. Second, our knot mass limit is an order of magnitude lower than that of the GALEX samples, leading to a corresponding increase in the number of identifications. Third, optical colors can, in principle, differentiate stellar populations that are several times older than those differentiated with the UV colors, thereby extending the baseline over which the phenomenon can be studied, and again increasing the sample size. If we can overcome the difficulty in distinguishing between stellar knots and background sources in optical images, high-quality ground-based data will provide a much greater number of knots, and potentially a larger sample of galaxies with such data, for any statistical analysis of outer disk properties.

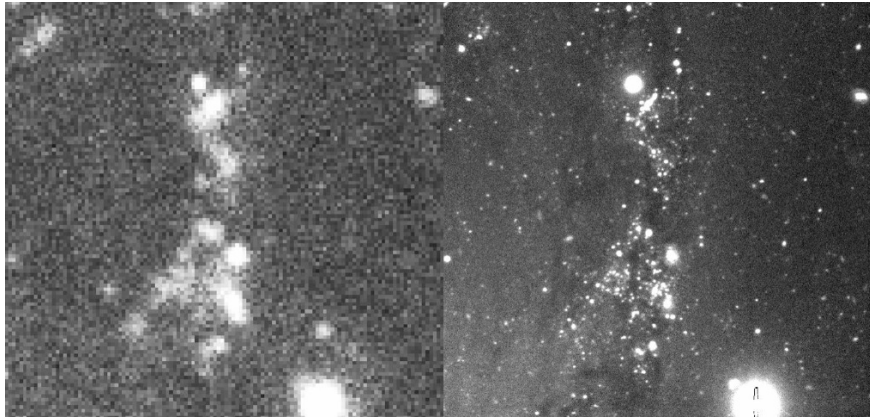


FIG. 1.— Comparison of GALEX (left) and LBT imaging (right) of a 3 arcmin-wide (4.1 kpc) region in the outskirts of NGC 4736.

The key to success lies in identifying some property, in addition to color, that can be used to disentangle the stellar clusters from background galaxies. Herbert-Fort et al. (2009) used the self-clustering of the outer disk knots to that effect and presented results for NGC 3184. Here we apply both the “classical” color approach and our self-clustering method to characterize these outer disk populations. With results drawn from these two approaches, we address questions regarding the ubiquity of outer disk knots, measure the knot formation rate, probe the radial extent of the knot distribution, and compare the distribution of knots to the H I distribution.

We present the results of a statistical study of nearby ( $< 15$  Mpc) outer disks, using the  $2 \times 8.4$ m Large Binocular Telescope (LBT; Hill et al. 2006) and wide-field, prime-focus Large Binocular Cameras (LBC; Ragazzoni et al. 2006; Giallongo et al. 2008). We describe our data reduction, develop analysis tools, and apply these to deep  $U$ -band and  $V$ -band imaging data of six galaxies. We demonstrate how the two separate statistical methods enable us to trace outer disk cluster-like objects to large radii. In §2 we describe our observations, data reductions and source detections. In §3 we present color-magnitude diagrams (CMDs) of candidate outer disk sources, quantify the range of properties consistent with the observed knots, and characterize the knot populations around galaxies. In §4 we describe the application of our restricted three-point correlation analysis of LBT knots, a similar analysis of GALEX knots, and a cross-correlation analysis of LBT knots and the underlying H I distribution. First, we present the different analyses, and then discuss them jointly on a galaxy-by-galaxy basis in §5. We summarize our results and conclusions in §6.

## 2. OBSERVATIONS TO FINAL SOURCE CATALOGS

We present new observations of six galaxies (IC 4182, NGC 3351, NGC 4736, NGC 4826, NGC 5474, NGC 6503) with the LBC-Blue imaging camera on the LBT on the dates listed in Table 1. These systems comprise a representative sample of nearby disk galaxies by spanning a range of physical disk sizes. All are nearby ( $D \sim 15$  Mpc) and only two, NGC 4826 and NGC 6503, are seen at high inclination ( $> 60^\circ$ ). For the four low inclination systems, their small distances and low inclinations allow us to measure the clustering of sources in the disk as a function of galactic

radius. We construct the final galaxy mosaics from many individual 164-second dithered exposures through the  $U$  and  $V$  Bessel filters (hereafter  $U$  and  $V$ ), except for NGC 5474, for which we combine 33-second dithered exposures in  $U$  to avoid saturating a bright star in the field. The typical seeing during our observations was  $0''.8$  and never exceeded  $\sim 1''.3$ . IC 4182, NGC 4736, and NGC 5474 were observed under photometric conditions. We obtained single photometric exposures for NGC 3351, NGC 4826, and NGC 6503 on 2/8/08 ( $U$  &  $V$ ), 4/20/07 ( $U$  &  $V$ ), and 4/22/07 ( $U$ ) & 4/7/08 ( $V$ ), respectively, for photometric calibration. We observed six photometric Landolt standard star fields (Landolt 1992) for flux calibration and all magnitudes are on the Vega system.

We follow the image processing steps described by Herbert-Fort et al. (2009). We use a set of Interactive Data Language (IDL<sup>1</sup>) scripts we created to construct ‘master bias’ frames that correct for global changes and the two dimensional structure in the bias level across the CCDs. We correct for sensitivity variations across the CCDs by combining dithered, twilight-sky flat-field images that are normalized by the four-chip median value of each bias-corrected flat field exposure. We then median-combine the normalized flats to create the master flat frames and, finally, divide the bias-corrected science frames by the master flats to complete the processing of the individual science exposures.

The target galaxies are well centered on the mosaic, so we sample the background of each exposure in twenty regions around the edges of the detector array. From these twenty regions we are able to obtain sufficient samples from which to judge the uniformity of the background and obtain an estimate of the uncertainty in our background estimate. The background is estimated using the IDL routine MMM<sup>2</sup>, which uses an iterative process to determine the mode of the sky values after rejecting outlying pixels (caused by stars, saturation, cosmic rays, hot pixels and bad columns). This step is done for each four-chip exposure and the minimum estimated sky from the various regions is subtracted from each corresponding chip. We then create a weightmap for every four-chip exposure to

<sup>1</sup>Developed by Research Systems, Inc. and owned by ITT; <http://www.itvis.com/ProductServices/IDL.aspx>

<sup>2</sup>Part of the Goddard IDL library, maintained by W. Landsman; <http://idlastro.gsfc.nasa.gov/>

mask bad columns (detected by eye in the master flats), hot pixels and cosmic rays (detected using the IDL routine REJECT\_CR, which finds features sharper than the PSF) when creating the mosaic images.

To combine the individual frames into final exposures we first use SExtractor (Bertin & Arnouts 1996) to create a source catalog for every exposure so that SCAMP<sup>3</sup> (Bertin 2006) can correct for optical distortions in LBC-Blue by solving the astrometry of the dithered exposures and creating smooth distortion maps for use by SWarp<sup>4</sup>. In cases where the SDSS fifth data release (DR5; Adelman-McCarthy et al. 2007) does not cover the science field, we use the USNO-B catalog (Monet et al. 2003) as the reference. We use SWarp to mean-combine the spatially-aligned frames after accounting for the bad pixel maps. Our final mosaic images are rebinned to a  $\sim 0''.22$  pixel<sup>-1</sup> spatial scale and have their photometry normalized to a fixed counts arcsec<sup>-2</sup> second<sup>-1</sup> standard. The mosaics are flat to 0.5 – 1% and have total integration times of  $\sim 25$  minutes in the deepest areas (see Table 1).

We build aperture photometry catalogs using SExtractor, with source detection and aperture placement based on the deeper *V*-band mosaic. We select sources by identifying groups of five or more pixels each with flux  $> 1\sigma$  above the background (so detections are in total  $> 3\sigma$ ). Because we detect the integrated light from members of stellar groups, the ‘knots’, any photometric algorithm that requires a uniform object shape for extraction is not optimal for this work. See Herbert-Fort et al. (2009) for all of the chosen SExtractor parameters. We detect nearly all visually discernable objects beyond the optical radius  $R_{25}$ , though our catalog becomes noticeably incomplete inside  $\sim 0.8R_{25}$ . Any algorithm will have difficulty detecting sources over the bright, extended emission of the inner disk. Issues regarding the completeness relative to our visual detections are negligible because the faint objects that are of interest in such a discussion are later rejected on the grounds of the low precision of their color measurement.

We use processed photometric exposures of Landolt standard star fields, taken on the same night as our individual photometric exposures of the galaxies, for calibration. We account for an airmass and a color term when flux-calibrating on the standard Vega system. Finally, we bootstrap the photometry of the photometric exposures to the deep mosaics using  $\sim 10$  stars common to both.

Colors and magnitudes are measured using circular apertures. Colors quoted throughout are from apertures with a diameter fixed to four pixels ( $0''.9$ , just larger than the typical  $0''.8$  FWHM of detected sources), while *V* magnitudes are apertures with a fixed 10 pixel diameter ( $2''.24$ ) that are then aperture corrected using stellar curves of growth (see Table 1 for those corrections,  $V_{corr}$ ). Aperture corrections were calculated from  $\sim 8$  isolated, unsaturated stars measured in 15 apertures spanning 2 – 50 pixels in diameter (or  $0''.4 - 11''.2$ ). We set SExtractor to mask and correct for contaminants. We check our photometry by comparing the *U* and *V* apparent magnitudes of ten well-isolated objects across the fields with those provided by SDSS-DR5 when available, otherwise USNO-B, converted from *u*, *g*, and *r* to either *U* or *V* using the transformations

of Jester et al. (2005). Aside from the systematic offset in our *V* magnitudes from NGC 4826 (see below), our results are consistent with the transformed SDSS photometry to within the transformed photometric errors.

The night of April 24, 2007 had poorer seeing than usual ( $\sim 1''.3$ ) during our *V* exposures of NGC 4826. As a result, the *U* – *V* colors of NGC 4826 sources, as estimated by eye from the CMDs presented in the next section, appear to be artificially blue by  $\sim 0.5$  mag relative to the source distributions of the other galaxies. This shift is as expected given the large aperture correction in *V* (Table 1) and the fact that the colors are aperture-matched (and hence not aperture corrected). A similar color offset, though of lower magnitude, is also just noticeable in the color-magnitude diagrams of NGC 5474 and NGC 6503 and these galaxies have the next highest aperture corrections. The solution to this problem is to PSF-match all the frames, but that would result in a significant degradation of the data. We choose not to apply the PSF matching because these color offsets do not impact our results. None of the subsequent discussion is predicated on precisely measured colors and NGC 4826 (the galaxy showing the strongest effect), as well as NGC 6503, are eventually dropped from the analysis because of their relatively high inclinations ( $i = 61^\circ$  and  $74^\circ$ , respectively).

To complete our final source catalogs, we reject sources whose internal *U* – *V* color error is  $> 0.5$  mag (magnitude errors are provided by SExtractor and propagated in the standard manner) and interactively mask regions around bright stars (those showing diffraction spikes and halos of scattered light) because the SExtractor catalogs have artificially low counts in those regions, which creates artificial structure in our correlation maps. In summary, our catalog is surface brightness limited due to the criterion on flux per pixel, magnitude limited due to the criterion on number of pixels above the particular surface brightness, and color limited due to the requirement of a modest uncertainty in the color measurement. The latter two in particular drive some of the structure seen in the color-magnitude diagrams discussed in §3. Our catalog is also subject to the confusion limit, although evidently at a finer resolution limit than GALEX (see Figure 1). We provide the number of sources in our final catalogs between  $1.0 - 1.5R_{25}$ ,  $1.5 - 2.0R_{25}$ , and  $2.0 - 2.5R_{25}$  and the area in each annulus after masking (Table 2). The chosen outer limit in this Table,  $2.5R_{25}$ , is somewhat arbitrary, loosely based on previous outer disk studies, for example Zaritsky & Christlein (2007).

### 3. OUTER DISK CLUSTER POPULATIONS

We will eventually appeal to our clustering analysis to tease out the most information regarding the distribution of the knots in the outskirts of these galaxies. However, it is worthwhile first examining color-magnitude diagrams to gain some intuition regarding the nature of the knots. The aim of this section is therefore not a detailed description of the knots, because we are dominated by uncertainties in accounting for the dominant background population, but rather a broad appraisal of the knots. Estimated masses and ages are highly uncertain.

In Figure 2, we present the color-magnitude diagram, CMD, of sources between  $1.0 - 1.5R_{25}$  in the field of IC 4182 and tracks from default Starburst99 (Leitherer et al.

<sup>3</sup>Version 1.4.0; <http://terapix.iap.fr/soft/scamp>

<sup>4</sup>Version 2.17.1; <http://terapix.iap.fr/soft/swarp>

1999; Vazquez & Leitherer 2005) that show the locations of model clusters of fixed mass and solar metallicity for ages between 1 Myr to 3 Gyr. We have also examined models with 1/5th and 1/50th solar metallicities. The 1/5th solar model is indistinguishable at the level of precision relevant for the qualitative conclusions we reach ( $< 0.5$  mag), and the 1/50 solar model differs significantly,  $> 1$  mag, but only for ages  $< 10$  Myr, at colors where we find few knots in most of our galaxies. Given current observational constraints (Werk et al. 2011), we do not expect outer-disk clusters to have extremely sub-solar metallicities. The upper and lower tracks represent  $10^4 M_\odot$  and  $10^2 M_\odot$  clusters, respectively, scaled from a simulated  $10^6 M_\odot$  cluster that adequately samples the upper mass range of a Kroupa IMF. Because we ignore the stochastic sampling of the IMF at low cluster masses (Cerviño & Luridiana 2004; Fagiolini et al. 2007), a simple comparison between data and the scaled model tracks can lead to an underestimate of cluster mass and an overestimate of the age. Therefore, these tracks are only meant to provide a general impression of the cluster masses and ages consistent with the range of sources in our sample.

More instructive are the background-subtracted Hess diagrams (Figures 3 — 8) that we create in the same manner as in Herbert-Fort et al. (2009), to statistically constrain the color and magnitude range of sources most likely to be clusters associated with each galaxy. A Hess diagram is a plot of the number of sources within color-magnitude bins (we use square bins of 0.2 mag here). For these particular diagrams, we create both a ‘background’ Hess diagram from a region far outside the galaxy and a ‘outer disk+background’ Hess diagram from the region of interest (say  $1.0 - 1.5 R_{25}$ ), scale the counts in the ‘background’ Hess diagram by the relative areas of the two regions, and subtract it, bin-by-bin from the ‘outer disk+background’ Hess diagram. The three panels in each Figure show the residual source density between  $1.0 - 1.5 R_{25}$  (left; dark regions are positive counts),  $1.5 - 2.0 R_{25}$  (middle), and

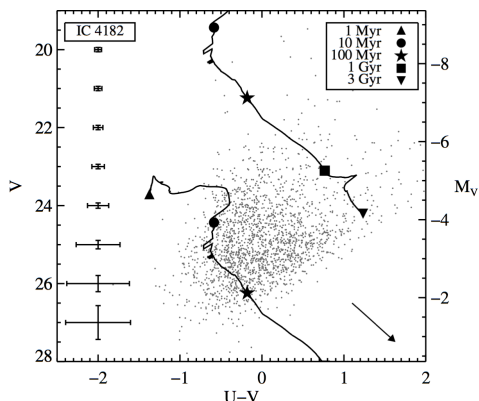


FIG. 2. — CMD of *all* sources surrounding IC 4182 (including background sources) between  $1.0 - 1.5 R_{25}$  (after masking areas around bright stars; see text), with median  $1\sigma$  errors as a function of apparent magnitude shown on the left. A reddening vector corresponding to 1 magnitude of extinction in  $V$ , calculated using results from Rieke & Lebofsky (1985), is shown at lower right. The work of Alberts et al. (2011) suggests low extinction in outer disks ( $E(B-V) < 0.3$ ). The tracks represent solar-metallicity  $10^3$  (lower) and  $10^6 M_\odot$  (upper) star clusters as a function of age. These tracks do not account for stochastic sampling of the stellar mass function. See §3 for more details.

$2.0 - 2.5 R_{25}$  (right). Solid and dotted black contours outline signal above and below the background, respectively, at  $> 90\%$  confidence level (CL), calculated using the low-count, Poisson single-sided upper and lower limits from Gehrels (1986). Because the solid contours surround pixels whose individual value is above the background at the 90% CL, groups of such pixels are detections at a much greater CL. Overplotted is a  $10^3 M_\odot$  Starburst99 model cluster, scaled from a  $10^6 M_\odot$  cluster, as shown in Figure 2. See Table 2 for source counts and other details of the Hess diagrams, including our estimates of the effective surface brightness of the outer disk cluster components.

All six galaxies show excesses in their background-subtracted Hess diagrams between  $1.0 - 1.5 R_{25}$ , roughly tracing the  $10^3 M_\odot$  cluster track. The tilted contours in the lower portion of all the panels reflects the color selection (bluer knots are visible to fainter  $V$  magnitudes). All galaxies except NGC 5474 show suggestive excess between  $1.5 - 2.0 R_{25}$ , though the noise is noticeably higher. We are skeptical, although not dismissive, of apparent excess between  $2.0 - 2.5 R_{25}$  because those diagrams are so strongly peppered with oversubtraction (nevertheless, the morphology of signal beyond  $R_{25}$  does follow that seen within  $R_{25}$ ). The principal source of uncertainty here are the variations in the background population. The effect of this can be seen in the appearance and disappearance of regions of oversubtraction, and in the change in location of such oversubtraction, within the various Hess diagrams. In contrast, the excesses seen in all six galaxies straddle the model track, lending credence to our association of such a signal with a physical, associated population of sources.

In Figure 9 we present the average Hess diagram for our six galaxies, with populations combined at constant  $M_V$ , with and without NGC 4736. We single out NGC 4736 because it is the nearest and largest galaxy (in angular extent) in our sample, resulting in a disproportionate number of detected sources and a less well-determined background level. These average Hess diagrams, either with or without NGC 4736, show convincing excess out to at least  $2.0 R_{25}$  in that there is more area enclosed within the solid contours than within the dashed contours (alternatively, based on Table 2, each galaxy has an average excess of over 70 knots between 1.5 and 2  $R_{25}$ , even if we exclude NGC 4736). We conclude that there is indeed a population of knots extending well beyond  $R_{25}$  in all of these galaxies and that the knots are consistent with a population of stellar clusters. We will now refer to these objects as stellar clusters. The exact distribution of masses and ages is difficult to disentangle from these plots given the uncertainties in the luminosities and colors of low mass clusters arising from the stochastic sampling of the stellar mass function, the uncertainties in the modeling, and the large uncertainties arising from the background subtraction.

### 3.1. An Estimate of the Cluster Formation Rate

To gain some intuition on the implied cluster formation rate from these diagrams and to further test our assertion that these are clusters, we simulate a population of  $10^3 M_\odot$  clusters forming at a specified constant rate over the previous several Gyr and plot the resulting Hess diagrams, accounting for the photometric uncertainties as estimated from the data for NGC 4736 (but not the uncertainties in

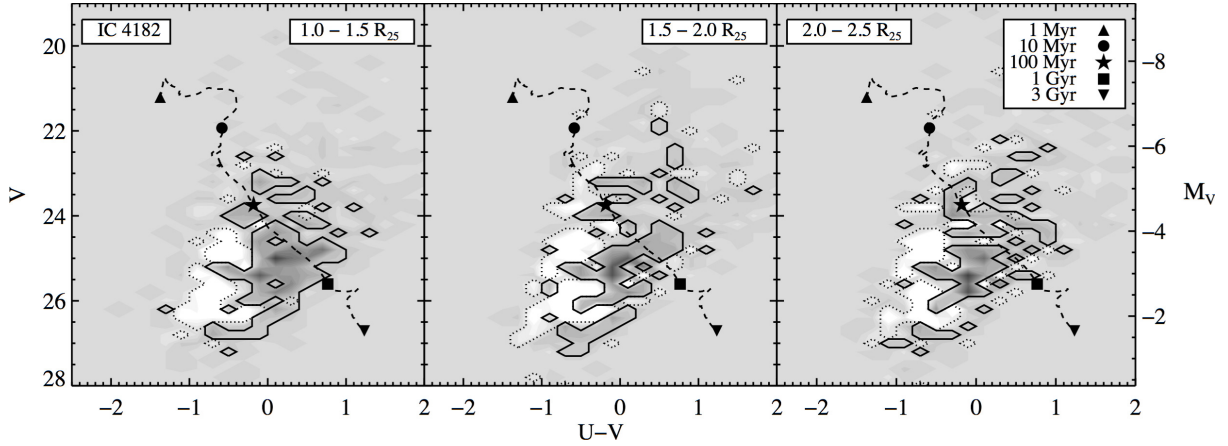


FIG. 3.— Background-subtracted Hess diagrams for IC 4182, made from sources between  $1.0 - 1.5 R_{25}$  (left),  $1.5 - 2.0 R_{25}$  (middle), and  $2.0 - 2.5 R_{25}$  (right). Dark regions represent positive counts. Solid and dotted black contours outline signal lying above and below the background at a  $> 90\%$  confidence level (CL), respectively; the dotted contours show any oversubtraction. Overplotted is a  $10^3 M_{\odot}$  Starburst99 model cluster, scaled down from a  $10^6 M_{\odot}$  cluster. Symbols represent the age of the cluster along the model sequence.

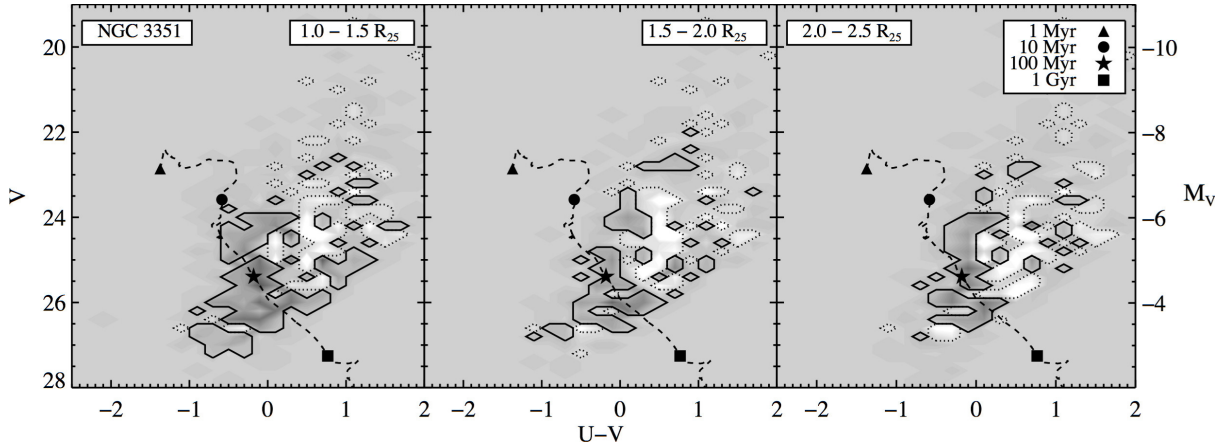


FIG. 4.— Same as Figure 3 but for NGC 3351.

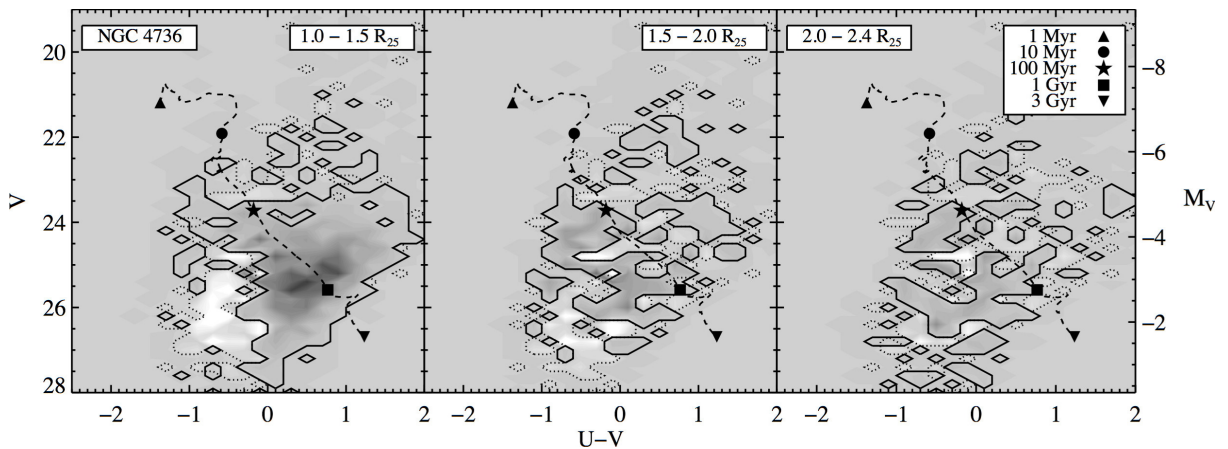


FIG. 5.— Same as Figure 3 but for NGC 4736.

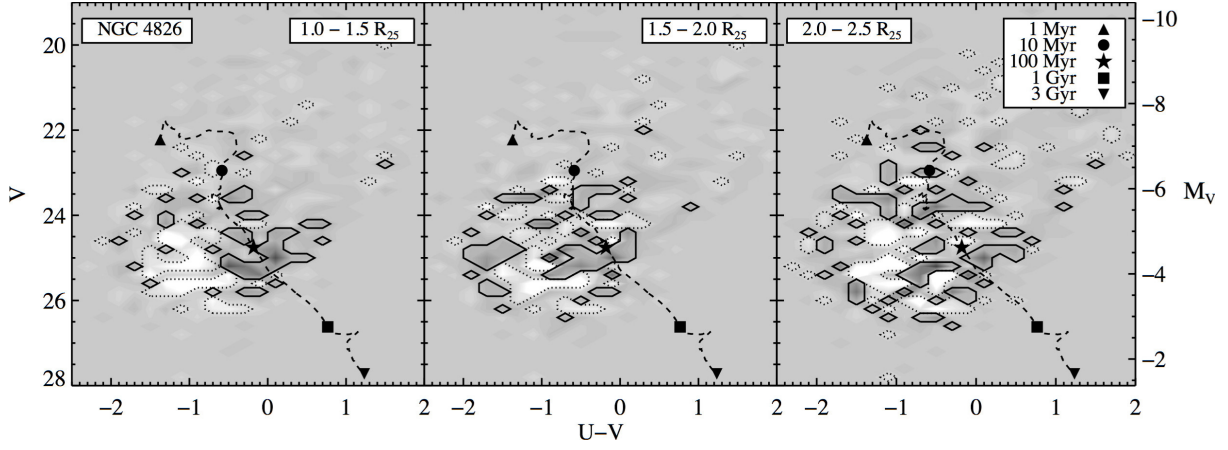


FIG. 6.— Same as Figure 3 but for NGC 4826.

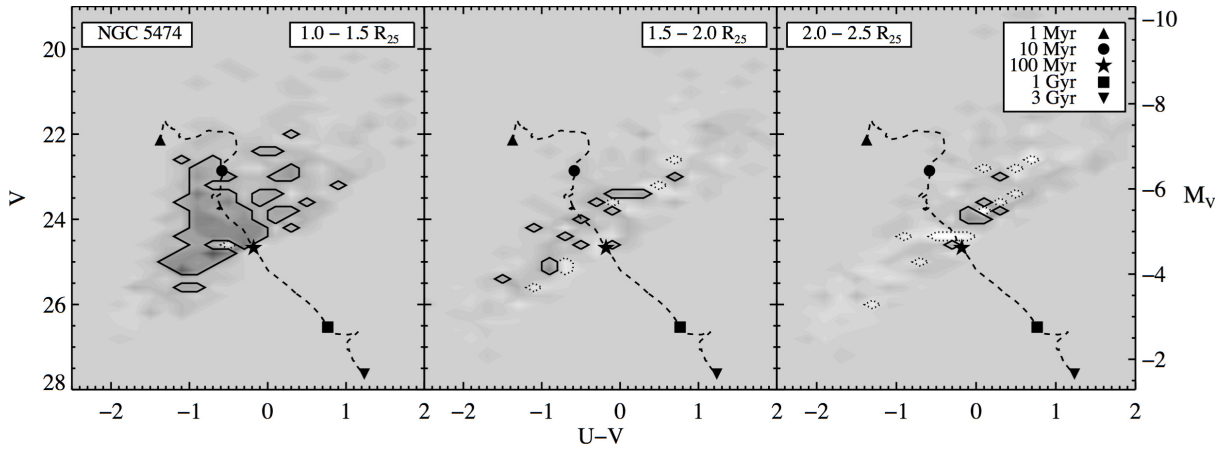


FIG. 7.— Same as Figure 3 but for NGC 5474.

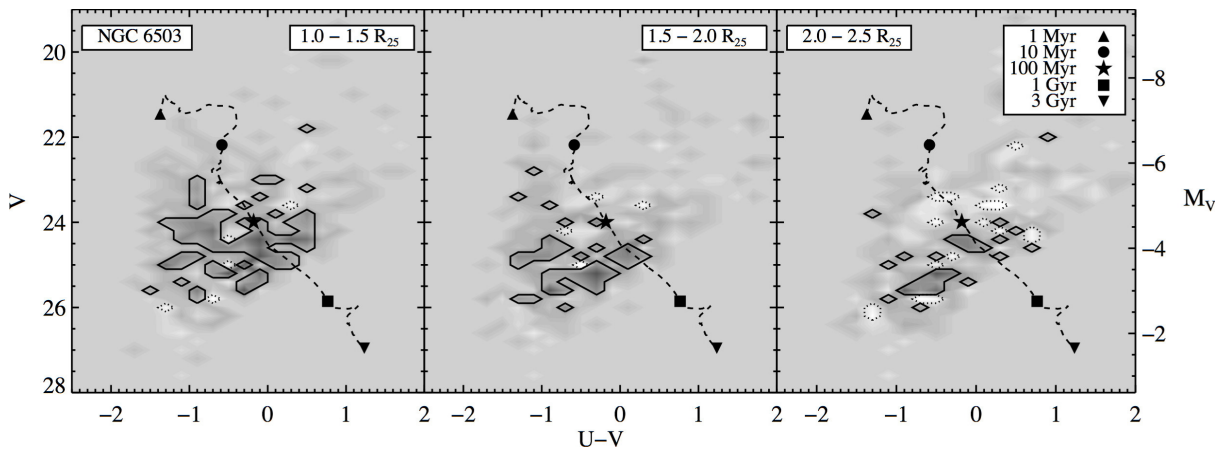


FIG. 8.— Same as Figure 3 but for NGC 6503.

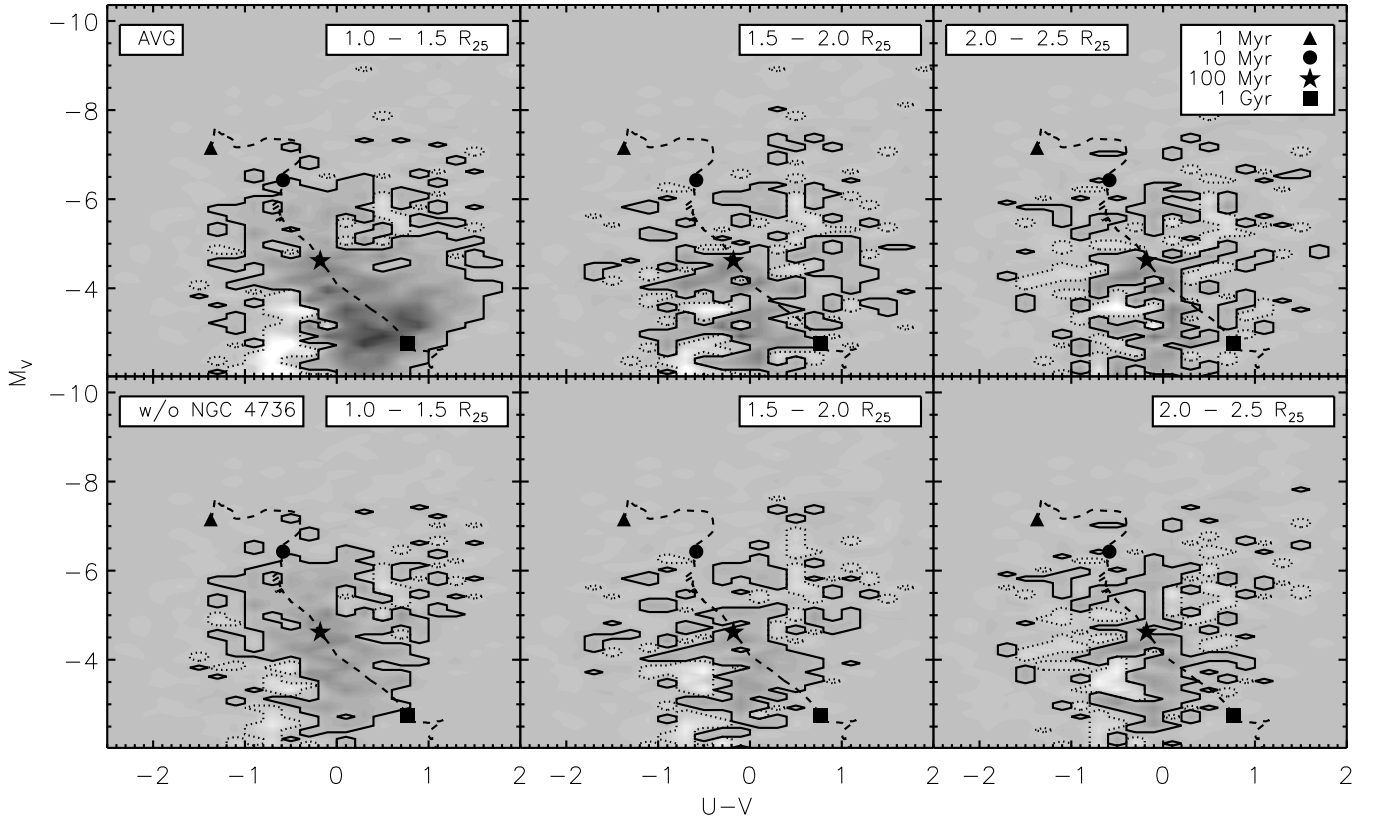


FIG. 9.— The average Hess diagram for all six galaxies, with sources combined as a function of  $M_V$ , including and excluding NGC 4736 (top and bottom panels, respectively). The three radial ranges are the same as in the individual Hess diagrams ( $1.0 - 1.5 R_{25}$ ,  $1.5 - 2.0 R_{25}$ , and  $2.0 - 2.5 R_{25}$ ). Dark regions are positive counts. Solid and dotted black contours outline signal lying above and below the background at a  $> 90\%$  confidence level (CL), respectively; the dotted contours show any oversubtraction. Overplotted is a  $10^3 M_\odot$  Starburst99 model cluster, scaled down from a  $10^6 M_\odot$  cluster. There is excess signal out to at least  $2 R_{25}$ .

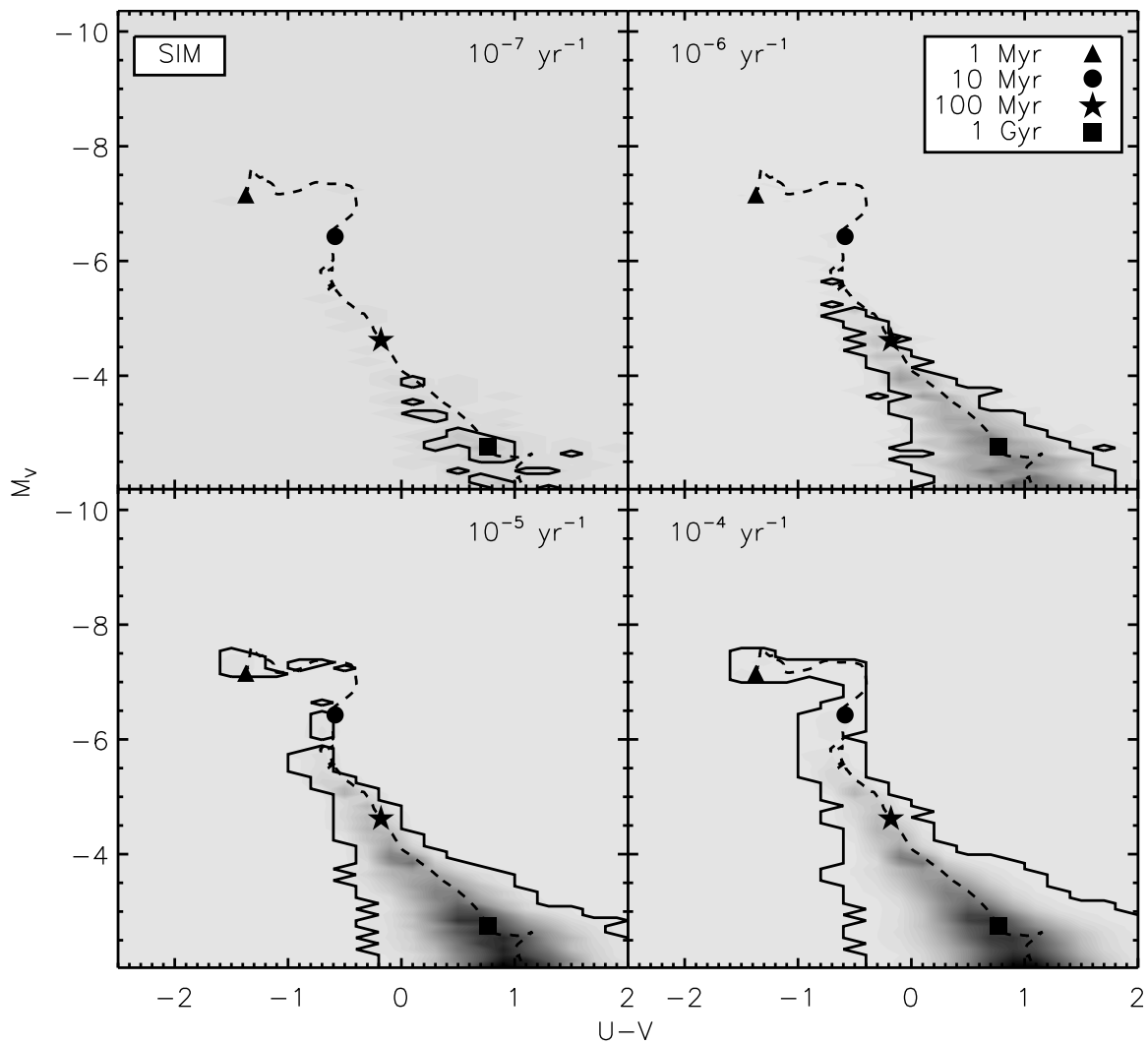


FIG. 10.— Simulated Hess diagrams made from a Starburst99  $10^3 M_{\odot}$  cluster track, with CMD uncertainties corresponding to those found for NGC 4736, for different cluster formation rates (top left: one every  $10 \times 10^6$  yr; top right: one every  $10^6$  yr; bottom left: one every  $10^5$  yr; bottom right: one every  $10^4$ ). No background is considered when making the simulated diagrams.



the background subtraction nor the stochastic sampling of the stellar mass function, in a figure analogous to Figure 9 for four different cluster formation rates. We assume no cluster dissolution or disruption, so this comparison will provide a lower limit on the cluster formation rate. Given the uncertainties in applying these models to the data, arising from the causes outlined above, this calculation is intended only as a plausibility argument for relating the knots to stellar clusters.

Comparing Figures 9 and 10, we conclude that the data exclude cluster formation rates significantly higher than one every  $\sim 10^6$  years for clusters of mass  $\geq 10^3 M_\odot$  (if there is no significant cluster dissolution) because we do not detect a population of blue sources at  $M_V \lesssim -7$  mag. This conclusion is relatively insensitive to the issue of stochastic sampling because that becomes less of a factor for the more massive clusters. On the other hand, rates significantly lower than  $10^{-6} \text{ yr}^{-1}$  fail to produce a sufficiently significant population of sources. This range of rates is consistent with a calculation where we simply take the number of outer disk knots in the  $1.0 - 1.5 R_{25}$  Hess diagrams ( $\sim 400$ ), the maximum age of a  $10^3 M_\odot$  cluster in our diagrams ( $\sim 1$  Gyr), and a uniform rate of formation over that time, which results in a rate estimate of one cluster every  $\sim 2.5$  Myr ( $4 \times 10^{-7} \text{ yr}^{-1}$ ). Converting this cluster formation rate to a stellar cluster mass rate implies that  $\sim 0.004 M_\odot \text{ pc}^{-2} \text{ Gyr}^{-1}$  is being tied up in stellar clusters at these radii (assuming  $R_{25} = 5$  kpc).

Alternative estimates of the outer disk cluster formation rate exist for comparison. Ferguson et al. (1998), using deep  $H\alpha$  imaging, measured the outer disk star formation rate densities of NGC 628, NGC 1058 and NGC 6946 to be between  $\sim 0.01 - 0.05 M_\odot \text{ pc}^{-2} \text{ Gyr}^{-1}$ . There are at least four potential explanations for our significantly ( $10\times$ ) lower formation rate, all of which probably contribute to the difference: 1) the cluster formation rates are highly stochastic and Ferguson et al. (1998) happened to catch these galaxies in an elevated phase relative to ours, 2) clusters disassociate, and so many are missing in our sample which samples older clusters, and 3) the  $H\alpha$  technique, which is sensitive to low mass clusters, is measuring a different mass component that happens to contain a larger fraction of the total mass, and 4) our estimates of the masses are significantly corrupted by our neglect of the stochastic effects and modeling uncertainties.

Regarding the first possibility, we know from a comparative study of GALEX knots (Zaritsky & Christlein 2007) that only a fraction of galaxies ( $\sim 25\%$ ) show significant overdensities of bright blue knots. If all galaxies have an outer disk population, as we seem to find on the basis of optical imaging presented here and spectroscopy (Christlein & Zaritsky 2008), then the formation rate must be highly variable (with a duty cycle of about 25% for GALEX-detectable knots). The effects of this stochasticity should be even more dramatic in  $H\alpha$ . Regarding the second option, we know that in certain environments where we have clusters spanning a range of ages, and can therefore do the study, that only a small fraction of all star clusters survive and we believe we understand the physical mechanism for this evolution (see Spitzer 1958; Gieles et al. 2011, and many related studies). Depending on the driver for cluster dissolution (mass loss versus

tidal stresses), the rate of cluster dissolution may be lower in the outer disks, but unlikely to be negligible. Davidge et al. (2011) find that clusters in the outer disk of M33 dissipate on a time scale of 100 Myr. The clusters we detect are  $\sim 100$  Myr old and older, and so likely to be a remnant population. This possibility is given further support by the recent work of Alberts et al. (2011), who in a set of five galaxies in which they are able to measure an age distribution of a set of massive ( $M \sim 10^5 - 10^6 M_\odot$ ), outer disk clusters, find that the age distributions are all peaked toward early times ( $\sim 100$  Myr and often within their innermost age bin of 50 Myr) even though they sample to ages of 1 Gyr. Finally, regarding the third option, Davidge et al. (2011) calculate that most of the outer disk clusters in M33 form at lower masses ( $50 - 250 M_\odot$ ) and so it may be the case that many of the  $H\alpha$ -detected clusters are of similar masses and below our detection threshold. It may also be the case that many of our clusters are low mass and boosted by stochastic effects into detectability. As such, any quantitative determination of the mass function of these clusters will require simulations that include detailed treatments of such effects, as well as of dynamical evolution and selection. Importantly, if we are missing 90% to 95% of the outer-disk cluster formation, as suggested by the Ferguson et al. (1998) results, then we must bear in mind that all of our subsequent estimates of stellar mass densities at these radii need to be multiplied by a factor of 10 to 20. For now, we ascribe the discrepancy to one of the effects described above rather than to a wholesale missing population from our catalog.

If the outer disks in our sample account for a star formation rates of  $4 \times 10^{-4} M_\odot \text{ yr}^{-1}$  (one  $10^3 M_\odot$  cluster every 2.5 Myr for  $1.0 R_{25} \leq R \leq 1.5 R_{25}$ ), then  $\sim 4 \times 10^6 M_\odot$  of stars have formed in that annulus over the lifetime of the galaxy (taken as  $10^{10}$  yr). As we discussed above, this is a lower limit since it ignores cluster dissolution and potential selection effects. If we multiply this number by 20, then we conclude that this limited region of the outer disk could contain as much as  $10^8 M_\odot$  of stars, or about 1% of the stars in a typical large spiral.

We conclude that adopting rough estimates of the typical mass and age of these clusters results in an outer disk star formation rate that is consistent with other estimates in that it lies below those other estimates. As such, our claim that these are indeed outer disk star clusters does not conflict with those other observations.

#### 4. CLUSTERING IN THE OUTER DISKS

The analysis of the color-magnitude diagrams are limited by the immense contamination from background objects. As we mentioned before, while at UV wavelengths that contamination is held in check, at optical wavelengths another method is needed to help differentiate outer disk clusters from background objects. To enhance the contrast between outer disk clusters and the background, we now utilize spatial correlations among the clusters and between the clusters and other detected, outer-disk components. First, we describe the self-correlation of LBT-knots. We will discuss the results for individual galaxies in detail, and the sample as a whole, in §5. Second, we present the application of the same technique to existing GALEX data for these same galaxies. In general, there are fewer GALEX knots per galaxy, so the statistical information is

poorer, but those data offer an independent check on our LBT results. Finally, we cross-correlate the position of the LBT-knots with the H I in an attempt to confirm tenuous evidence for very distant clusters through their association with neutral hydrogen at these large radii.

#### 4.1. Self-clustering of LBT Knots

Following Herbert-Fort et al. (2009), we present restricted three-point correlation maps to trace the self-clustering of knots in the outer disks (see Figure 11 for a description of the radii used). The self-clustering of outer disk clusters provides an enhanced contrast relative to the background (which has a different angular correlation function). Instead of measuring a radial profile of detected sources and subtracting some average background level, which is simply related to the azimuthally-averaged two-point correlation function (e.g. Zaritsky & Christlein 2007), here we use the self-clustering of knots to highlight regions with clusters and remove signal from large-scale background fluctuations. This technique only measures the extent of *clustered* knots; stars or clusters in a diffuse component, even if originally born in clustered clusters, will evade detection. Therefore, we stress that any null detection does not indicate a lack of stellar populations at large galactic radii.

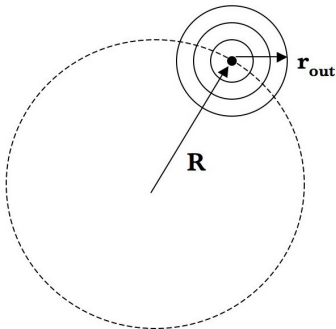


FIG. 11.— The radii defined for creating the restricted three-point correlation maps. The center of the parent galaxy lies at the origin and the dot represents one outer disk knot. The original description of this method, along with this figure, are presented by Herbert-Fort et al. (2009).

The restricted three-point correlation maps of our four low-inclination galaxies ( $i < 60^\circ$ ) are presented in Figures 12 – 15. The top panels are constructed using all detections (the ‘All’ sample) with  $-1.7 < U - V < 0.7$  and  $19 < V < 27.5$ , while the lower panels result from splitting the samples into blue and red components on either side of  $U - V = -0.2$  (middle and bottom panels, respectively, and comprise the ‘Blue’ and ‘Red’ samples). Black and gray show areas where signal is detected at the  $> 95\%$  and  $> 99\%$  significance level, respectively, as a function of both galactic radius  $R$  and intercluster radius  $r_{out}$  (Figure 11). The confidence levels are determined as described by Herbert-Fort et al. (2009) using a Monte-Carlo approach. The dotted lines show the radial extent of H I for  $N(\text{H I}) > 2 \times 10^{20} \text{ cm}^{-2}$  (left, at  $r_{out} = 0 \text{ kpc}$ ) and for  $N(\text{H I})$  above the noise level of the integrated H I map (right, at  $r_{out} = 0 \text{ kpc}$ ). The dotted lines are slanted to distinguish the  $[R, r_{out}]$  regions that can be populated by sources within the H I disk. The H I data and analysis are described later in the paper.

The interpretation of these Figures is somewhat unusual so we outline the salient features. Positive signal at any location is potentially a marker of clustering. However, positive signal at low  $r_{out}$ , which is typically seen interior to  $R_{25}$  is a sign of small-scale, tight clustering of stellar clusters. Vertical bands, which are seen at a variety of radii, suggest a set of clusters at a particular radius that may not be strongly clustered, such as those in a spiral arm or ring. Because of the nature of the axes, a fixed amount along the vertical axis represents a much larger angle at a smaller  $R/R_{25}$  than at a larger one, but we expect clustering to depend on physical separation rather than on angular separation.

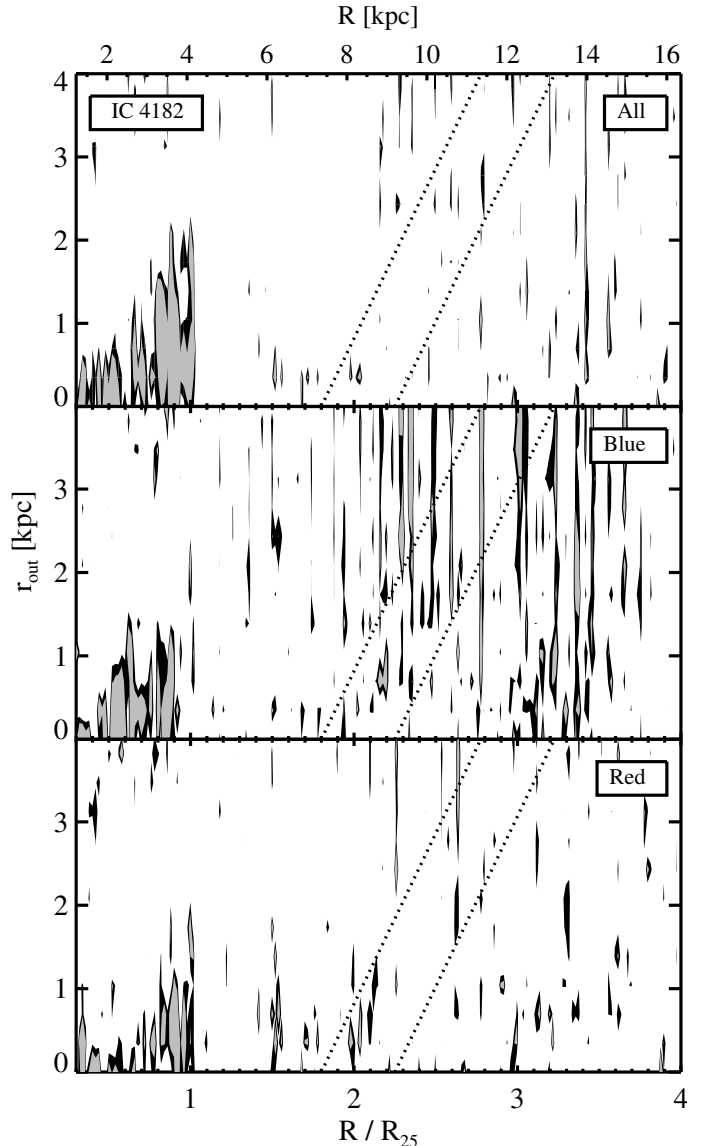


FIG. 12.— Restricted three-point correlation maps from sources in our (masked) final catalog of IC 4182. Black and gray show areas where signal is detected at the  $> 95\%$  and  $> 99\%$  significance level, respectively, as a function of both galactic radius  $R$  and intercluster radius  $r_{out}$  (Figure 11). The dotted lines show the radial extent of H I for  $N(\text{H I}) > 2 \times 10^{20} \text{ cm}^{-2}$  (left, at  $r_{out} = 0 \text{ kpc}$ ) and for  $N(\text{H I})$  above the noise level of the integrated H I map (right, at  $r_{out} = 0 \text{ kpc}$ ). The dotted lines distinguish the regions where knots could be co-located with the H I (left and right of the dotted lines, respectively).

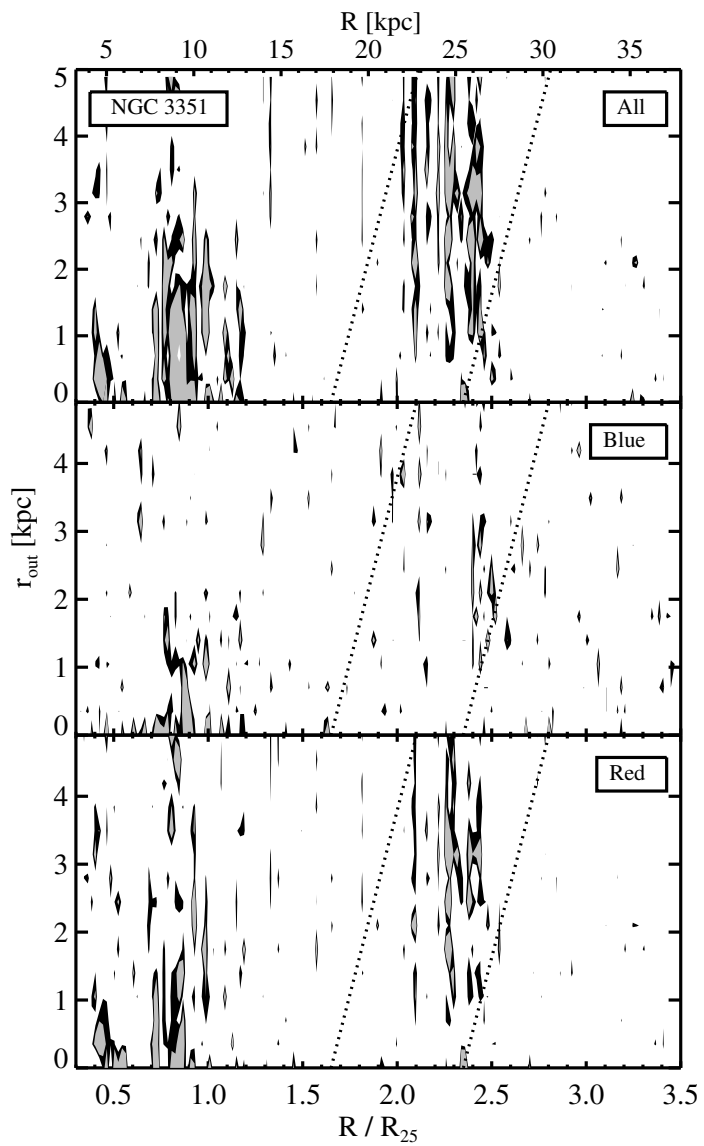


FIG. 13.— Same as Figure 12 but for NGC 3351.

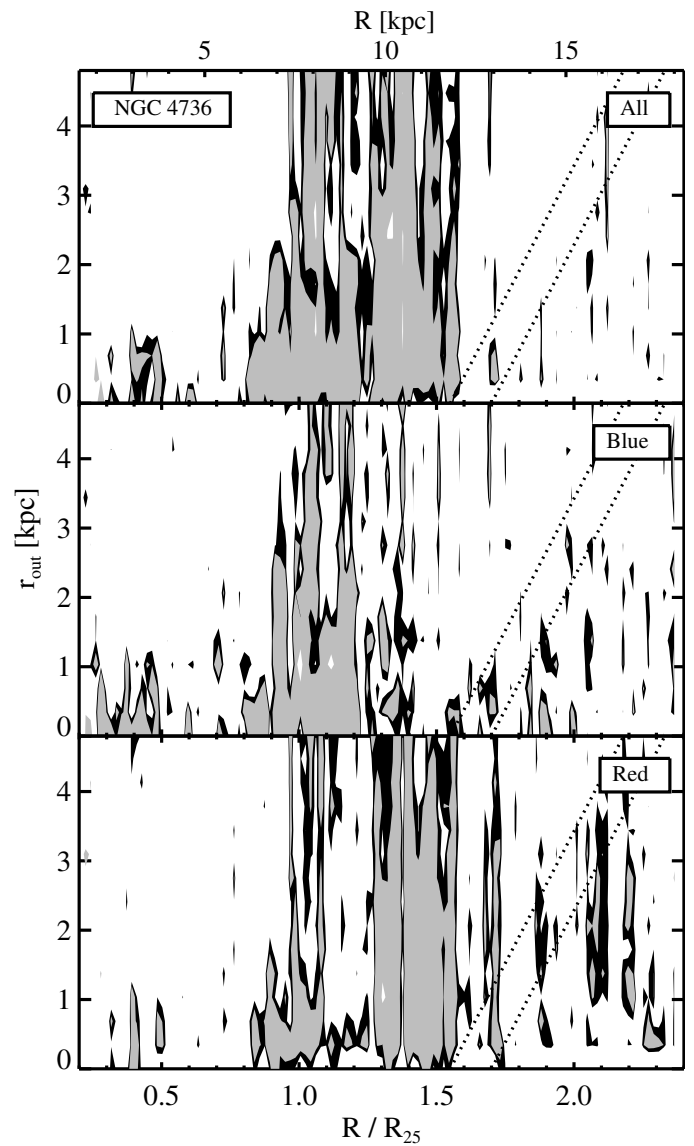


FIG. 14.— Same as Figure 12 but for NGC 4736.

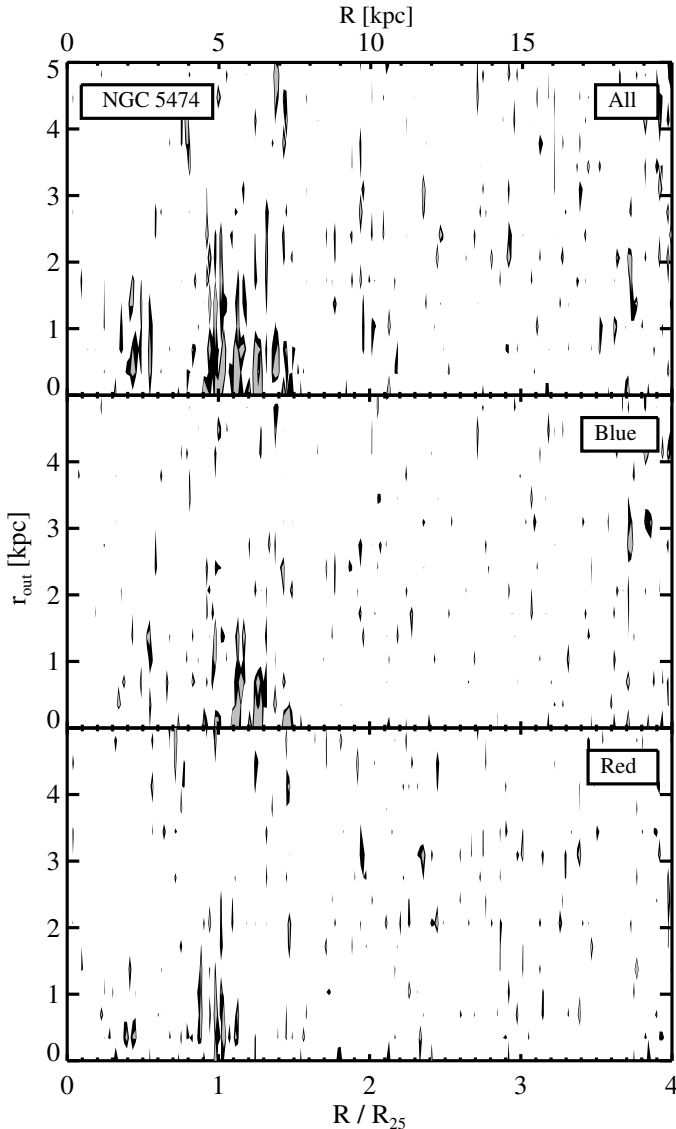


FIG. 15.— Same as Figure 12 but for NGC 5474.

Reaching conclusions regarding the radial extent of correlated clusters from these maps is difficult because of the irregular nature of the signal and the statistical fact that given enough pixels some will randomly host  $3\sigma$  variations. Rather than judge the significance of correlation peaks by eye, we calculate at each radius whether the occurrence of outliers is statistically beyond what is expected. For this calculation, we use probabilities calculated using binomial statistics with the appropriate probability corresponding to that of the unlikely event (for example, we calculate the likelihood of having as many as  $M$  or more pixels out of  $N$  pixels hosting ‘true’ values if the probability of obtaining a true value is 0.1). We rebin our data in the  $R$  direction so that each element now corresponds to a  $\Delta R$  of the same size as the  $\Delta r_{out}$ , so that each element is independent.

We calculate the probability of finding as many ‘significant’ detections in the correlation maps by chance as a function of galactocentric radius, over the range of  $r_{out}$  plotted in the correlation maps ( $\sim 5$  kpc), and present the results in Figures 16 — 19. The black and gray lines correspond to the black and gray signal in the correlation maps. The dotted lines indicate the same H I extents as in the correlation maps. Black or gray signal below the dashed line at  $-2.568$  indicates concentrations of correlation signal that are highly unlikely ( $> 3\sigma$ ) to be generated by chance (i.e. the correlation signal excess is statistically significant).

Before discussing the results of our LBT correlation maps and the corresponding probability plots, we present a similar correlation analysis of GALEX knots around these same galaxies and a cross-correlation analysis of our LBT knots and the underlying H I distribution. We then discuss the results of these three analyses together, on a galaxy-by-galaxy basis. We do this because comparison to independent data provides additional credence to our detections.

#### 4.2. Self-clustering of GALEX Knots

We now apply our three-point correlation analysis to the distribution of UV-bright knots around our galaxies, using data from publicly available GALEX catalogs. If the outer disk regions that we detect in the LBT data are continuing to form clusters, then we might detect corresponding GALEX knot self-clustering (i.e. GALEX knot - GALEX knot clustering). Such a detection would not only confirm what may be marginal detections in the LBT data, but also provide information on the timescales of spatially localized cluster formation and cluster dispersal.

When possible, we combine the GALEX catalogs from shallow ( $t_{exp} < 1000$  seconds) and deep exposures to include sources both near and far from the bright inner galactic disk (regions around the galaxies were masked in the catalog generation for the deep GALEX exposures and so the shallow exposures help fill in the source distribution). We then cut the combined GALEX source lists to match the ‘blue’ sample of Zaritsky & Christlein (2007) with  $FUV-NUV < 1$  and  $NUV < 25$ , corresponding to clusters younger than  $\sim 360$  Myr. This cut removes sources with detections in only one GALEX band and retains the most reliable knots. We reduce contamination further by only retaining knots that match sources in our LBT catalogs (to within  $3''$ , roughly half a GALEX resolution element). The large majority,  $> 90\%$ , of the GALEX

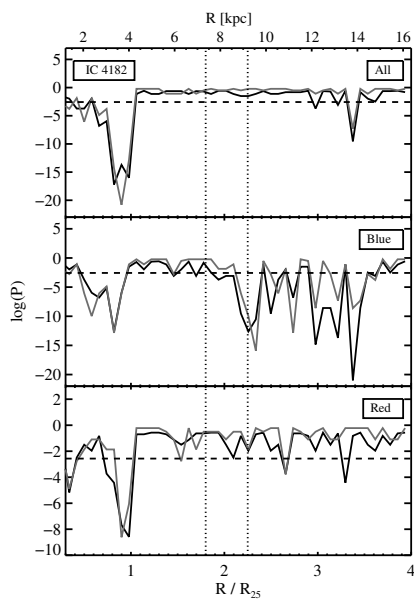


FIG. 16.— Probability, as a function of radius, that signal in the three-point correlation map of IC 4182 (Figure 12) is due to random excursions. The black and gray lines correspond to the black and gray signal in the correlation map. The dotted lines indicate the same H I extents as in the correlation map. Black or gray signal below the dashed line at  $-2.568$  indicates concentrations of correlation signal in Figure 12 that are very unlikely ( $> 3\sigma$ ) to be generated by random noise.

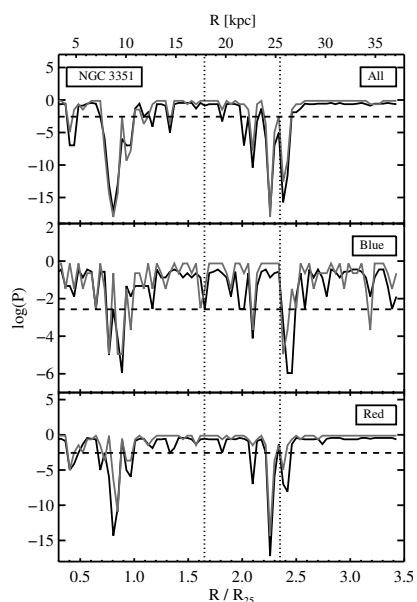


FIG. 17.— Same as Figure 16 but for NGC 3351.

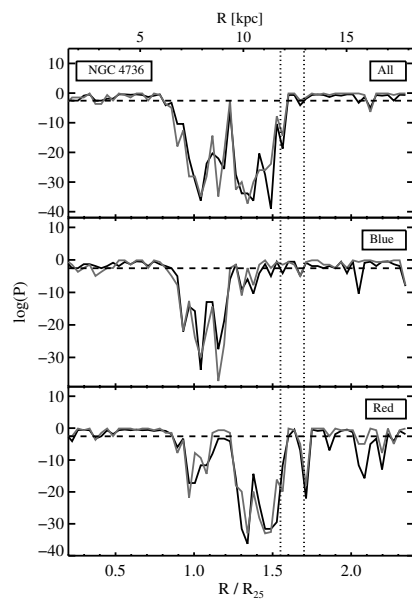


FIG. 18.— Same as Figure 16 but for NGC 4736.

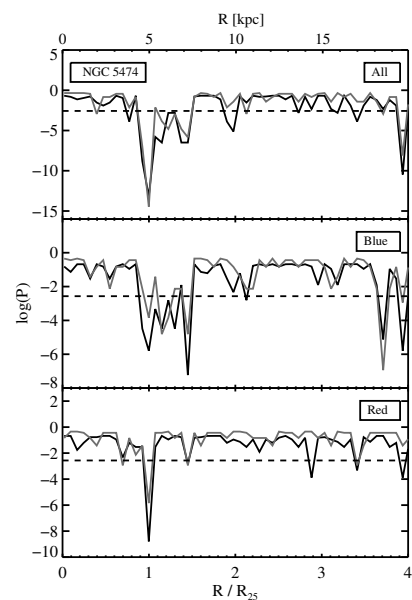


FIG. 19.— Same as Figure 16 but for NGC 5474.

knots positionally match an LBT source.

Before proceeding to the correlation analysis, we compare the number of GALEX knots around each galaxy with those remaining in the background-subtracted Hess diagrams (Figure 3 – 9) and present the results for two outer disk annuli in each low-inclination galaxy, between  $1.0 - 1.5R_{25}$  and  $1.5 - 2.0R_{25}$ , in Table 3. Unfortunately, the inner annulus is problematic because the GALEX catalogs near the disk are made from shallow exposures. In the  $1.5 - 2.0R_{25}$  annulus, we find that GALEX knots make up between 10%-40% of LBT knots, or 27% on average. For a population of clusters that form continually, this ratio should simply reflect the timescales over which the clusters would be detected in GALEX versus LBT imaging, if cluster dissolution affects both samples similarly. Since dissolution is expected to proceed very rapidly (few million year timescale; see Fall, Chandar, & Whitmore 2005) both the GALEX and LBT samples, unlike  $H\alpha$  samples, are dominated by clusters that ‘survive’. The average age of the GALEX population is  $\sim 180$  Myr (assuming a uniform distribution of ages between 0 – 360 Myr, where the upper bound is set by the UV color selection), while that of the LBT clusters is  $\sim 500$  Myr (assuming a uniform distribution between 0 – 1 Gyr, where the upper limit is again given by the color and magnitude selection). The ratio of these mean ages leads to an estimated fraction of 36%, sufficiently close to our detected average of 27% that we cannot rule out the hypothesis of continual cluster formation. A lower fraction implies a higher cluster formation rate in the past, while a higher fraction implies a lower formation rate. The observed scatter between 10% - 40% suggests that factor of two variations in the cluster formation rate over these timescales are likely, but that the rates do not change by orders of magnitude over the previous Gyr when integrated over timescales of  $\sim 200$  Myr (roughly the resolution limit of our crude age estimates).

We present the UV knot self-clustering maps from our final GALEX source catalogs in Figures 20 to 23. Unfortunately, the number of available GALEX sources is low; 171 were used around IC4182, 179 around NGC 3351, 398 around NGC 4736, and 174 around NGC 5474. Of these, NGC 4736 and NGC 5474 were included in the Zaritsky & Christlein (2007) study. They found an excess of knots in both cases, although the probability of the excess being random is not exceedingly small, 4% for NGC 4736, so the results based solely on the radial distribution of GALEX knots are marginal. Interestingly, the LBT results for NGC 4736 are the strongest in our optical sample, and so show the value of going to deeper, redder samples in uncovering outer disk populations.

#### 4.3. Cross-correlation of LBT Knots and Neutral Gas Disks

We now compare the distribution of our LBT sources to the neutral gas distribution. This cross-correlation provides another way to constrain the extent of the stellar disks, particularly in relation to the known component that stretches to the farthest radii. Any association between the  $H\ I$  structure and knots is also key for understanding how star formation arises in this environment.

Once again, because we perform an angular cross correlation analysis, we are restricted to our low-inclination

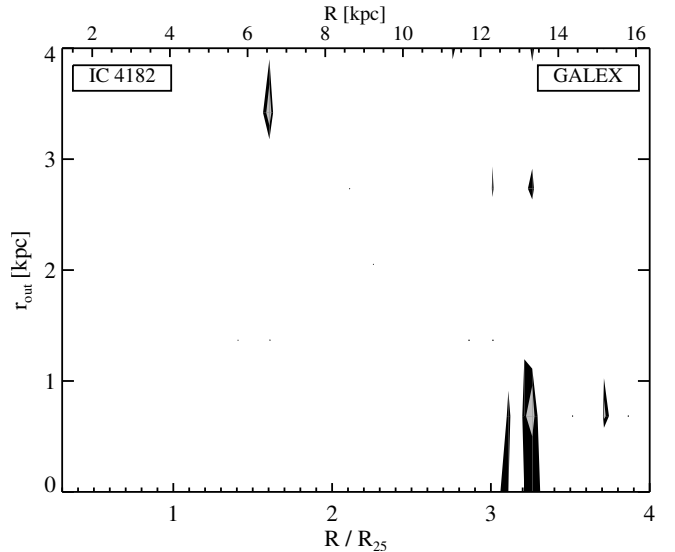


FIG. 20.— Restricted three-point correlation map similar to Figure 12 but here using 171 GALEX sources around IC 4182. The statistics are limited in comparison to the LBT self-clustering analysis by the relative shallower depth and poorer resolution of GALEX.

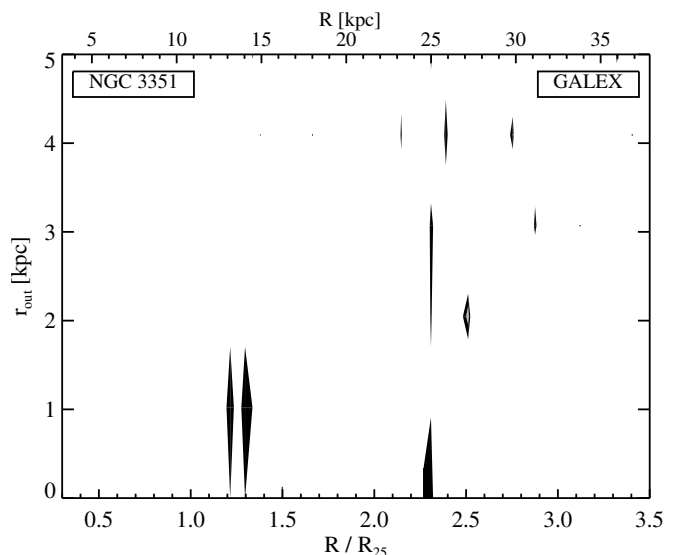


FIG. 21.— Same as Figure 20 but from 179 GALEX sources around NGC 3351.

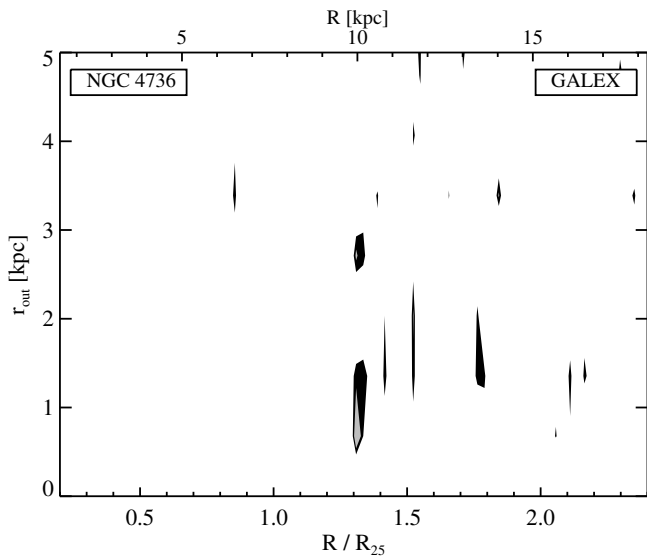


FIG. 22.— Same as Figure 20 but from 398 GALEX sources around NGC 4736.

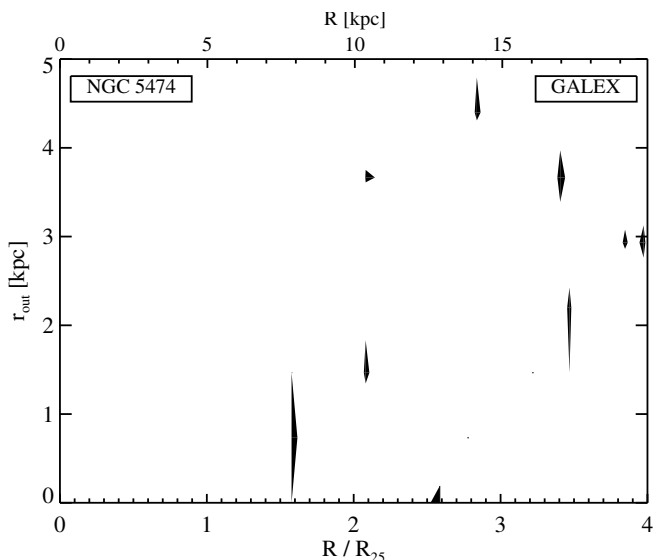


FIG. 23.— Same as Figure 20 but from 174 GALEX sources around NGC 5474.

sample (IC 4182, NGC 3351, NGC 4736, and NGC 5474). A further limitation is that we do not have a suitable H I map of NGC 5474. The integrated H I (moment 0) maps for NGC 3351 and NGC 4736 come from The H I Nearby Galaxy Survey (THINGS; Walter et al. 2008) and for IC 4182 from the H I map of from the Westerbork H I Survey of Spiral and Irregular Galaxies (WHISP; Swaters et al. 2002). We estimate the extent of the gas in the same manner as described by Herbert-Fort et al. (2009), by examining histograms of the number of H I pixels per  $\text{kpc}^2$  above a certain  $N(\text{H I})$  threshold, as a function of  $R$  in  $0.025R_{25}$ -wide elliptical annuli.

The first threshold we consider is the noise level of the H I maps (see below), to determine the maximum detected extent of the gas in each of the three galaxies. The ‘noise level’ of the final H I maps results from already having cleaned the maps, only keeping pixels where two or more adjacent channels show significant signal ( $2\sigma$ ) in the integrated moment 0 map (so the ‘noise level’ here is really more significant than the ‘ $2\sigma$ ’ noise level in the raw data). The neutral gas around IC 4182 extends to  $\sim 2.25R_{25}$  around IC 4182, to  $\sim 2.4R_{25}$  around NGC 3351, and to  $\sim 1.8R_{25}$  around NGC 4736. Figures 24 — 26 show the restricted three-point cross-correlation between the LBT knots and the H I pixels lying above the  $N(\text{H I})$  threshold (listed in the legend at the bottom right of each panel). The top panels show results using the ‘All’ sample while the lower panels give the results from using the ‘Blue’ and ‘Red’ samples (middle and bottom panel, respectively). Black and gray show areas where signal is detected at  $> 95\%$  and  $> 99\%$  significance, respectively. The dotted lines bracket the radial extent of the H I pixels used. The Figures show that LBT knots correlate with H I features out to, and beyond, the observed edges of the gas disks. As Herbert-Fort et al. (2009) discussed, the vertical bands of signal highlight likely spiral arm structures.

To determine what H I density might be the best tracer of knot formation, we focus on our ‘Blue’ LBT knot sample and calculate correlations relative to the H I distribution as defined by different column density thresholds. Figures 27 — 29 contain results specifically for  $N(\text{H I}) > 1.0 \times 10^{20} \text{ cm}^{-2}$  (middle), and  $N(\text{H I}) > 2.0 \times 10^{20} \text{ cm}^{-2}$  (bottom). The highest threshold,  $N(\text{H I}) > 2.0 \times 10^{20} \text{ cm}^{-2}$ , corresponds to where one finds damped Lyman- $\alpha$  (DLA) absorption, and so, distinguishes regions that contain predominantly neutral or ionized gas (see Wolfe et al. 2005, and references therein). The  $N(\text{H I}) = 2 \times 10^{20} \text{ cm}^{-2}$  threshold highlights the edge of the dominant reservoir of neutral gas. The  $N(\text{H I}) = 1.0 \times 10^{20} \text{ cm}^{-2}$  threshold was determined by eye to be the lowest density value at which the contours closely trace the distribution of the ‘Blue’ knots. The radial extent of the H I decreases as the column density threshold increases, though as the density threshold is increased we are more likely selecting H I structures that could host cluster formation — unless the gas has been consumed to make the clusters or dispersed after cluster formation. Broadly, we find correlations between the knots and the gas at all gas densities and at all radii. We discuss individual cases and reach conclusions next.

## 5. RESULTS FOR INDIVIDUAL GALAXIES

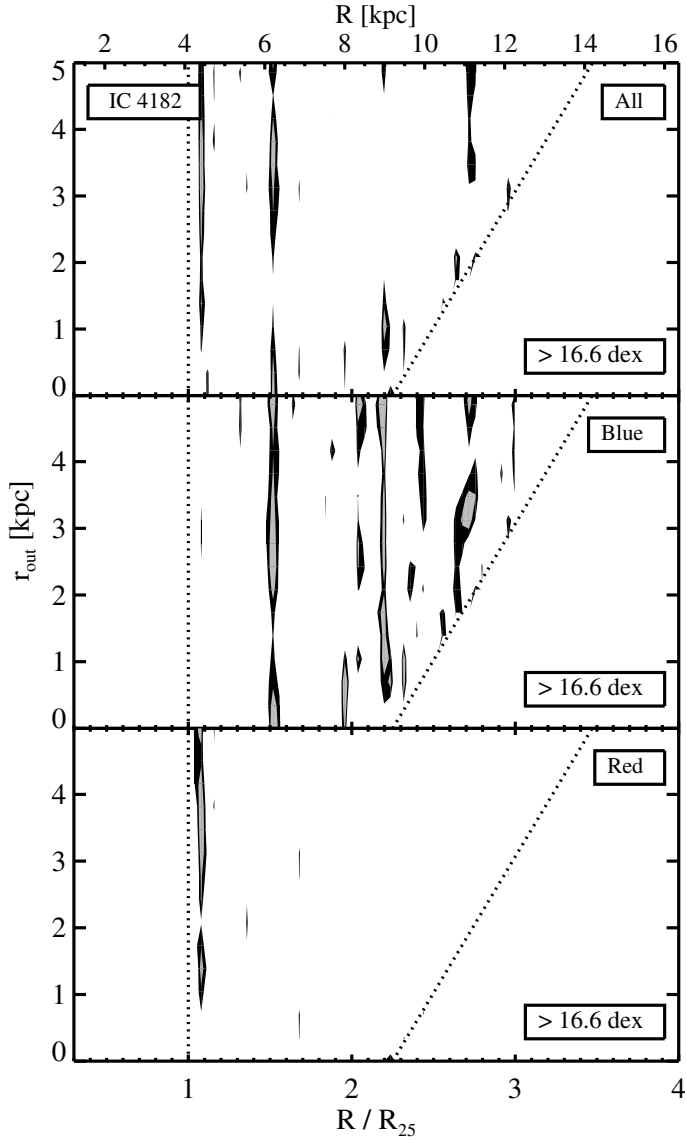


FIG. 24.— Restricted three-point cross-correlation maps of LBT-detected knots around IC 4182 and H I pixels with  $N(\text{H I})$  above the noise level of the integrated H I map ( $N(\text{H I}) > 4.0 \times 10^{16} \text{ cm}^{-2}$  here). The dotted lines bracket the radial extent of the H I pixels used; because no H I pixels exist beyond the dotted line on the right, we will not see signal at low  $r_{out}$  beyond this furthest H I radius (this explains the diagonal nature of signal at the largest  $R$ ). Only knots between  $1.0 - 3.0R_{25}$  were used.

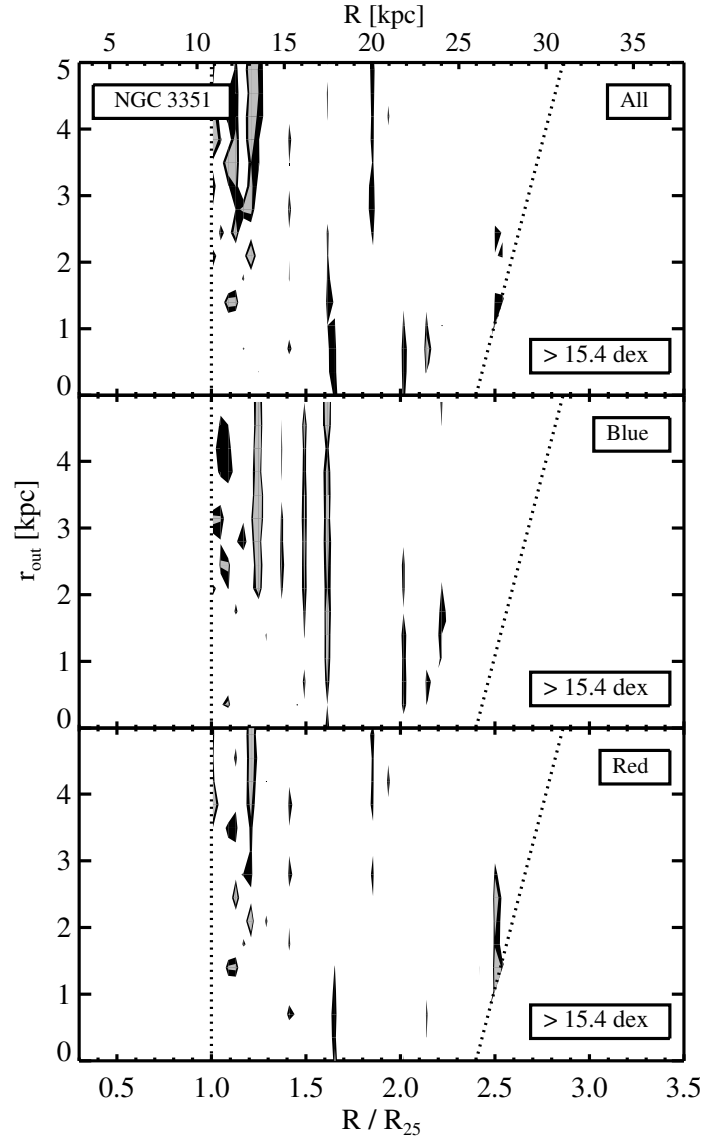


FIG. 25.— Same as Figure 24 but for NGC 3351. Only sources between  $1.0 - 3.5R_{25}$  were used.



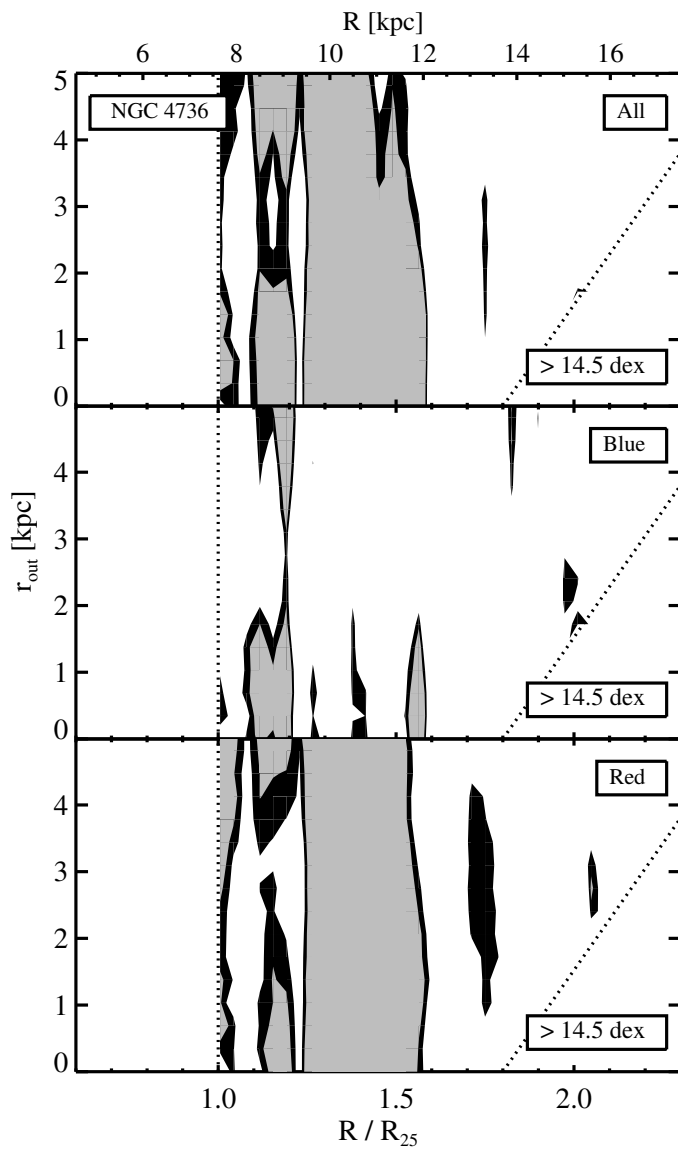


FIG. 26.— Same as Figure 24 but for NGC 4736. Only sources between  $1.0 - 2.2R_{25}$  were used.

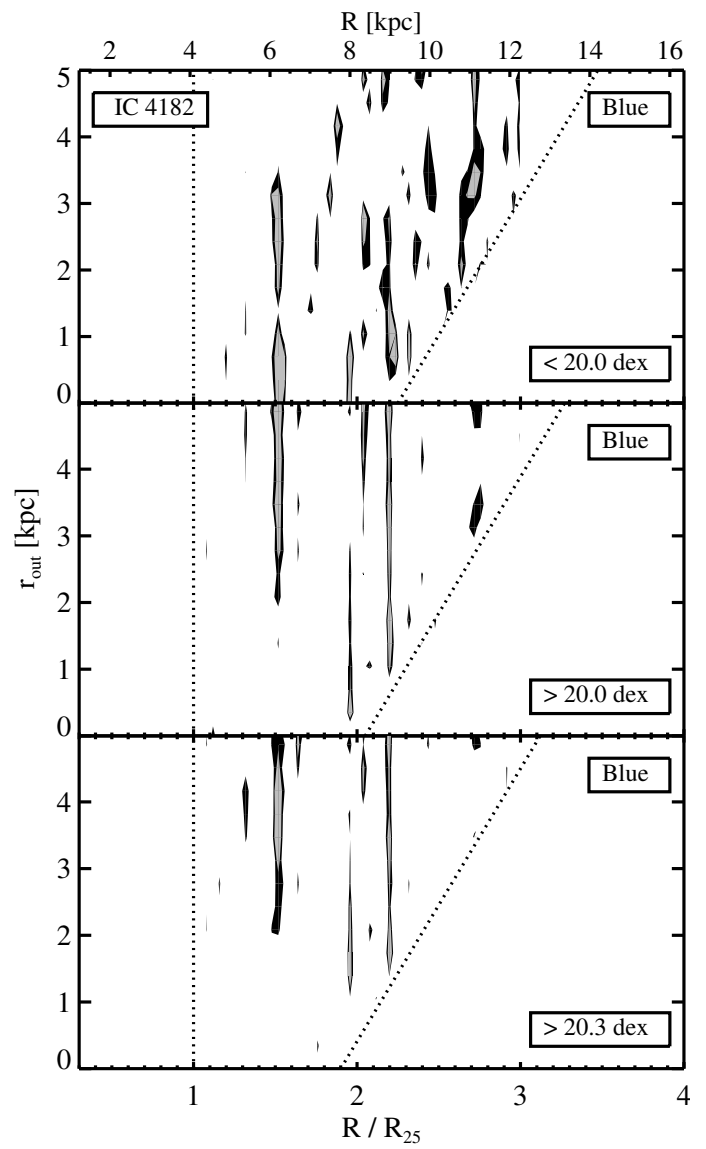


FIG. 27.— Same as Figure 24, but only for the Blue sample of IC 4182 and for different  $N(\text{H I})$  thresholds.

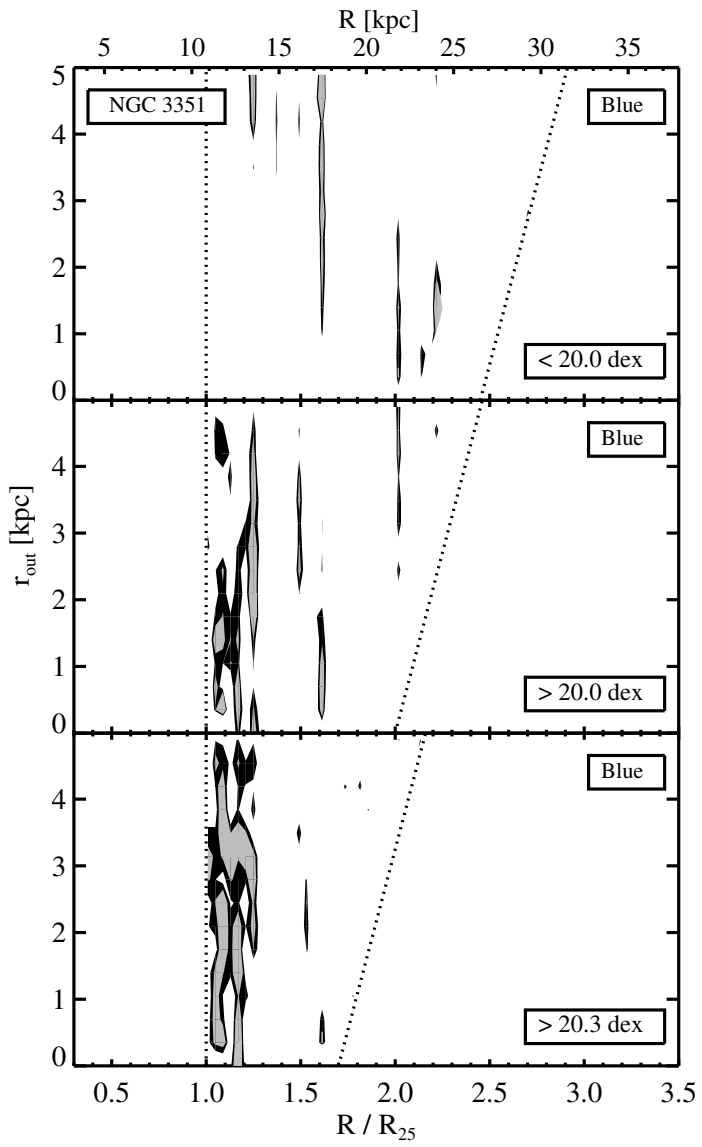


FIG. 28.— Same as Figure 27 but for NGC 3351.

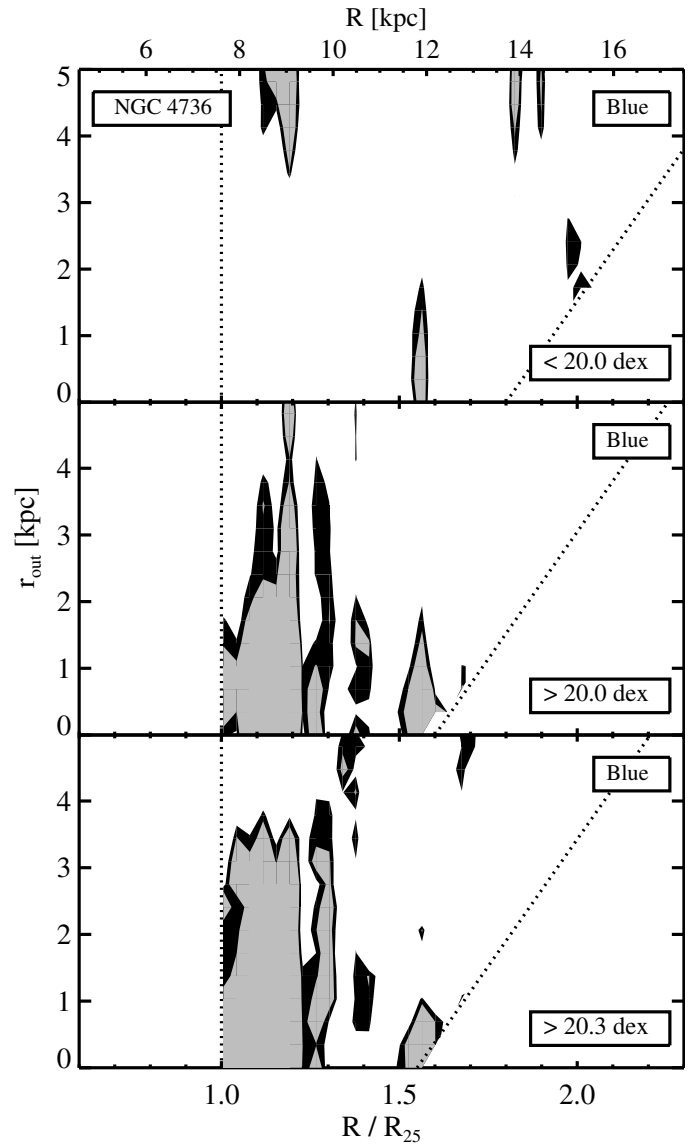


FIG. 29.— Same as Figure 27 but for NGC 4736.

A few general comments before we discuss the galaxies individually. In all four LBT correlation maps (Figures 12 — 15) there is significant signal at very large radii, in three cases extending beyond the H I (we do not have H I data for the fourth galaxy, NGC 5474). Though we are somewhat skeptical of correlation signal at such large radii, where the background becomes relatively more important, these detections may point to stars formed beyond the current edge of the observable H I disk. We examined the galaxy images and, with one exception that we discuss below, could not visually identify groupings of LBT knots at radii beyond the H I extent. However, the knots can be very difficult to find when they are far from the disk, not strongly clustered, and faint, which is of course why we devised the restricted 3-pt correlation analysis. When we compare correlation maps made using the masked and unmasked source distributions (masked to limit the catalog problems near bright stars, as mentioned in §2), much of the signal beyond the H I changes significantly in character, suggesting it might be artificial. We hesitate to increase the masking beyond what we already chose because of the limitation in the number of sources near the mosaic edges. Nevertheless, although some of the most distant signal may be artificial, we will demonstrate that some of the features are real and that there are clusters out to at least  $\sim 3R_{25}$  and beyond the edge of the H I disk. We now discuss the results for each galaxy.

#### 5.0.1. IC 4182

We find the bulk of the signal contained within  $\sim R_{25}$  in the LBT knot correlation map, although there is a great deal of structure in the Blue knot correlation map at larger radii, and some concentration of signal toward low  $r_{out}$  in the Red one (Figure 12). Working our way out in radius, the first tantalizing detection in the 2-D plot is in the Red knots at about  $\sim 1.5R_{25}$ . However, this turns out to not be statistically significant (Figure 4.2) and is also likely to be the remnant of structure caused by a bright star at that radius. However, strong signal exists near  $1.5R_{25}$  in the All and Blue panels of the LBT knot - H I cross-correlation plot (Figure 24). The lack of a self-clustering signal among the Blue sample is not counter-evidence, just evidence for a lack of strong self-clustering among such clusters. Interestingly, the Blue LBT knot - H I cross correlation at  $1.5R_{25}$  is most closely related to the lower-density gas,  $N(\text{H I}) < 20.0$  dex (Figure 27), suggesting that these knots have either moved away from the regions of highest gas density or affected their nearby environs.

Further out in  $R$ , the Blue panel of the LBT knot probability plot (Figure 16) shows more noisy, scattered signal beyond the edge of the H I than do the All or Red panels. This ‘noisy’ Blue signal in the LBT correlation map between  $2 - 3R_{25}$  is statistically significant in the probability plot and coincides with bands of Blue signal in the LBT knot - H I cross-correlation plots, suggesting that Blue clusters a few kpc beyond the edge of the gas are nevertheless strongly associated with the outer disk gas structure. This result suggests that the knots were either born from gas that was once part of the disk, but no longer exists, or that they have drifted somewhat in radius from their birth-sites. A drift velocity of just  $6 \text{ km s}^{-1}$  could transport a cluster a few kpc in 500 Myr. The GALEX correlation plot

(Figure 20) does not contain signal at these radii, which suggests that these clusters are somewhat older than a few hundred Myr. This scenario is consistent with the inferences discussed above that the clusters are not as strongly correlated with the highest density gas and that they may have drifted in radius.

Finally, all of the panels in the LBT knot correlation probability plot (Figure 16) show significant excess signal at  $\sim 3.3R_{25}$ , far outside the edge of the gas disk (the gas extends to  $2.2R_{25}$ ). This feature is especially interesting because it corresponds to strong signal at the same radius in the GALEX knot self-correlation map (Figure 20). Examining the GALEX image, we visually identify a clump of sources at that radius. If these distant sources are in fact outer-disk clusters, rather than a grouping of UV-bright background objects or stellar clusters in a satellite galaxy, they are very interesting objects for further study. H $\alpha$  imaging, and subsequent spectroscopy would be particularly valuable.

#### 5.0.2. NGC 3351

The bulk of the signal in the LBT knot correlation map and corresponding probability plot (Figures 13 and 17) is once again contained within  $\sim R_{25}$ , demonstrating that the optical radius does demarcate a real qualitative change in the nature of star formation. Again moving out in radius, the most significant signal comes in at around  $2.4R_{25}$  in the All and Red panels, and to a lesser degree in the Blue panel. These clusters are also seen in the GALEX correlations (Figure 21). Evidence for correlation between this population and the H I is weaker, although there is some signal near  $2.2R_{25}$  in the Blue panel and  $2.5R_{25}$  in the Red panel (Figure 25). This signal occurs right at the edge of the H I disk.

In addition to the clusters seen at the periphery of the H I, there is also signal in the LBT knot - H I cross-correlation map from  $R_{25}$  out to  $1.6R_{25}$ . From the Blue LBT knot - H I cross-correlation map for different  $N(\text{H I})$  thresholds (Figure 28), we conclude that the knots trace the denser gas out to  $\sim 1.6R_{25}$  (and trace spiral structure out to  $1.2R_{25}$ ). As in IC 4182, the bands of correlations between the Blue knots and H I come at semi-regular radial spacings, suggestive of multi-armed spirals with small pitch angles or rings.

#### 5.0.3. NGC 4736

As we have discussed before, NGC 4736 is by far the richest of our galaxies in outer disk structure and may therefore not be representative. Nevertheless, we see many of the same general patterns. The LBT knot correlation map and corresponding probability plot for NGC 4736 (Figures 14 and 18) show signal extending to at near the limit of the HI disk ( $\sim 1.6R_{25}$ ). This galaxy has an obvious overdensity of knots in the bright ‘ring’ surrounding it. Trujillo et al. (2009) found that this ring is actually a complex structure of wound spiral arms (perhaps caused by secular processes in the inner disk), which perhaps are a much stronger version of the low pitch angle arms we discussed in the context of IC 4182 and NGC 3351. The knots toward the inner edge of the outer disk are associated with higher density H I, as is also the case for NGC 3351. We are somewhat skeptical of excess signal beyond

the H I extent of this galaxy (signal at  $R \sim 2R_{25}$ ) because it is coincident with artificial signal that faded when we applied additional bright star masking, though there is some signal in the H I correlation maps at the same radius. The lack of correlation in the GALEX data is not a concern because the signal in the LBT correlation maps comes primarily from the Red sample.

#### 5.0.4. NGC 5474

NGC 5474 is our lowest noise LBT knot correlation map and contains significant signal from  $R_{25}$  to  $\sim 1.4R_{25}$  (Figures 15 and 19). Unfortunately, we do not have the same quality H I data for NGC 5474 as for the other three galaxies. However, the GALEX knot correlation map contains some signal near  $1.5R_{25}$ , though it is very weak (Figure 23). There are two reasons why the signal might be weak. First, it is possible that the GALEX knots do not cluster very tightly (or do not cluster differently than the background). Second, it may be that the relative small number of GALEX knots limits the degree to which this restricted 3-pt correlation can result in a statistically meaningful detection. From looking at the GALEX images and source distribution we conclude that this feature is real, but this weak signal (as well as the rather tame GALEX signal for NGC 4736) demonstrates how our optical work complements the GALEX studies.

There are a few marginally significant detections at intermediate radii in the correlation probability plot (Figure 19). A potentially interesting detection is that in the All panel at a radius slightly below  $2R_{25}$ . This radius matches our estimate for the outer extent of H I based on Figure 2 from Rownd et al. (1994). While the other three galaxies in our sample all show clear signs for cluster formation near the periphery of their H I distribution, we only have this questionable detection for NGC 5474.

In the outer extremity of the correlation maps,  $R \sim 3.5$  to  $4 R_{25}$ , we again find strong signal in the three knot populations. There is no corresponding signature in the GALEX maps (although we saw above that the GALEX detections can be weak) and, unfortunately, we do not have H I maps of the required quality to help confirm these features. The feature near  $4R_{25}$  is likely residual signal from a few bright stars at that radius.

## 6. SUMMARY AND CONCLUSIONS

We summarize our results as follows:

- All disk galaxies have a cluster population beyond  $R_{25}$ . The six for which we present background subtracted Hess diagrams show significant populations out to at least  $1.5R_{25}$ . The outer disk we studied similarly before (NGC 3184; Herbert-Fort et al. 2009) also contains this population. Many of our galaxies show similar populations extending to  $2R_{25}$  and occasionally beyond. We attribute the larger fraction of galaxies with detected outer disk populations relative to previous studies (Thilker et al. 2007; Zaritsky & Christlein 2007) to the superior mass and age sensitivity of the LBT data.
- Using the distribution of sources in the Hess diagrams, we infer that the typical detected cluster has a mass of  $\sim 10^3 M_{\odot}$ , is predominantly  $< 1$  Gyr old, and as a population have an average formation rate of at least  $\sim$  one cluster every 2.5 Myr. The corresponding rate of stellar

mass being formed in these clusters is  $\sim 0.004 M_{\odot} \text{ pc}^{-2} \text{ Gyr}^{-1}$  (assuming  $R_{25} = 5$  kpc and  $10^3 M_{\odot}$  clusters) for the area of the disk between  $R_{25}$  and  $1.5R_{25}$ . These estimates are rough, and may be systematically biased due to uncertainties in the modeling, stochastic effects in low mass cluster, and selection. The principal aim of this exercise was to demonstrate the plausibility of associating the detections with stellar clusters. Comparing the numbers of sources identified to the corresponding numbers found using GALEX, which is sensitive only to younger clusters, we conclude that the formation rate of clusters at these radii is constant, to within a factor of roughly 2, over the last Gyr.

- To further quantify the distribution of outer disk clusters, we construct restricted three-point correlation maps in our four low-inclination galaxies. We confirm many of these detections using comparisons of GALEX detected populations and correlations with H I. Again, we detect signal in all four, but our detections come in three varieties. First, we generally find a population of clusters that extends modestly beyond the optical radii (to between  $1.3$  and  $1.5 R_{25}$ ). Second, we find a population of clusters near the edge of the H I distribution. Lastly, in all but NGC 3351, we find detections of clusters well beyond the H I edge. These last are the most difficult to confirm independently (they could either be an unfortunate clustering of background sources or they could belong to satellite galaxies).

- From the cross-correlation signal between our Blue LBT-detected knots and the H I distribution we find two types of behavior. First, the knots near the optical edge of the disk are best traced by the higher density neutral gas, as one might expect in a steady state situation where density waves continually lead to the generation of new clusters. The pattern of the correlations, semi-regular bands in Figures 24 to 26, also suggest spiral arms, in this case with small pitch angles. Second, the knots farther out in the disk are most strongly correlated to the low density H I gas, suggesting that while some connection between star formation and fuel exists, the process is sufficiently transient and/or disturbing that correlations with high density gas do not persist.

From these results, as well as those presented in previous studies of outer disks, we suggest that outer disk cluster formation occurs in three modes. First, spiral waves from the inner disk continue beyond the optical radius and trigger continual, but low level, cluster formation out to at most  $\sim 1.5R_{25}$ . We have presented some evidence for this mode of cluster formation, but it can also be clearly seen in the H $\alpha$  images of NGC 628 (Ferguson et al. 1998) where the arms can be visually traced beyond  $R_{25}$ . Second, a global mode, where clusters are formed throughout the disk, is triggered by interactions. This mode is responsible for the rare and most dramatic examples of outer disk star formation, such as that seen in M83 (Thilker et al. 2005). Lastly, and most speculative, is a mode that creates clusters at the periphery of the H I disk. We suggest that this is where gas that is accreted joins the already existing gas and that this process leads to low level cluster formation. We consider these radii to represent the outer banks of galaxies, where the waves of incoming gas break upon the shores of the existing disk and leave telltale

‘foam’ upon their arrival.

This work relied on the invaluable `idlutils` software library developed by M. R. Blanton, S. Burles, D. P. Finkbeiner, D. W. Hogg, and D. J. Schlegel, and on the Goddard IDL library maintained by W. Landsman. We thank the THINGS and WHISP teams that produced the H I maps used here. We thank the referee for suggestions that clarified the text. DZ and SHF were partially supported under NASA LTSA NNG05GE82G and NSF AST-0307482. DZ thanks Cambridge University and New York University for their hospitality during the final stages of this work.

TABLE 1  
SAMPLE GALAXIES

Name	$i$ [deg]	PA [deg]	D [Mpc]	R25 [kpc]	$U_{date}$	$U_{exp}$ [sec]	$V_{date}$	$V_{exp}$ [sec]	$V_{lim}$	$V_{acor}$	$\sigma_{V_{acor}}$	Ref.
IC 4182	23	90	4.7	4.1	5/11/07	1640	5/11/07	1640	27.0	-0.11	0.05	1
NGC 3351	40	13	10.1	10.8	3/21/07	1640	3/21/07	1640	27.0	-0.15	0.05	4,5,6,7
NGC 4736	8	122	4.7	7.6	2/21/07	1640	2/21/07	1476	27.5	-0.13	0.03	2,3
NGC 4826	61	115	7.5	10.2	2/10/08	1476	4/24/07	1476	26.0	-0.69	0.04	1,8,9
NGC 5474	26	132	7.2	5.0	5/10/07	328	5/10/07	1804	26.0	-0.26	0.01	1,10
NGC 6503	74	121	5.3	4.5	4/23/07	1312	4/11,23/07	3280	26.0	-0.46	0.01	1,11,12

References. — 1: Karachentsev et al. (2004); 2: Karachentsev (2005); 3: Trujillo et al. (2009); 4: Graham et al. (1997); 5: Rubin et al. (1975); 6: Buta (1988); 7: Swartz et al. (2006); 8: Tonry et al. (2001); 9: Nilson et al. (1973); 10: Rownd et al. (1994); 11: Makarova (1999); 12: Begeman et al. (1987)

TABLE 2  
SOURCES IN COLOR-MAGNITUDE AND BACKGROUND-SUBTRACTED HESS DIAGRAMS

Name	Annulus [ $R_{25}$ ]	Area [arcmin <sup>-2</sup> ]	$N_{CMD}$	$N_{Hess}$	Fraction [%]	$\mu_{eff}$ [mag arcsec <sup>-2</sup> ]
IC 4182	1.0 – 1.5	30.95	1950	248	13	29.62
	1.5 – 2.0	41.66	2244	-48	...	30.44
	2.0 – 2.5	43.91	2408	-7	...	29.98
NGC 3351	1.0 – 1.5	40.22	2037	448	22	> 32.44
	1.5 – 2.0	38.22	1593	83	5	> 34.91
	2.0 – 2.5	37.52	1554	72	5	> 31.12
NGC 4736	1.0 – 1.5	85.38	8517	2774	33	29.46
	1.5 – 2.0	104.88	7570	516	7	30.43
	2.0 – 2.4	83.93	6135	489	8	> 30.99
NGC 4826	1.0 – 1.5	40.42	1445	-33	...	30.00
	1.5 – 2.0	52.90	1964	30	2	33.11
	2.0 – 2.5	72.15	2670	33	1	31.34
NGC 5474	1.0 – 1.5	19.96	699	427	61	28.85
	1.5 – 2.0	27.95	433	52	12	> 33.57
	2.0 – 2.5	35.93	465	-25	...	32.14
NGC 6503	1.0 – 1.5	8.69	622	369	59	28.36
	1.5 – 2.0	9.94	554	265	48	28.94
	2.0 – 2.5	13.63	511	114	22	29.75

Fraction is undefined when  $N_{Hess}$  is negative (there is no excess of disk sources over the background).  $\mu_{eff}$  is given as a lower limit when the total flux in the Hess diagram is negative. Note that there exist cases where  $N_{Hess}$  is negative but the total flux is not. This depends on the distribution of signal across the entire Hess diagram.

TABLE 3  
SOURCES IN LBT-MATCHED GALEX CATALOGS

Name	Annulus [ $R_{25}$ ]	$N_{GALEX}$	$N_{Hess}$	Fraction [%]
IC 4182	1.0 – 1.5	5	348	1
IC 4182	1.5 – 2.0	28	69	41
NGC 3351	1.0 – 1.5	12	548	2
NGC 3351	1.5 – 2.0	27	266	10
NGC 4736	1.0 – 1.5	56	2738	2
NGC 4736	1.5 – 2.0	172	704	24
NGC 5474	1.0 – 1.5	8	427	2
NGC 5474	1.5 – 2.0	16	52	31

Because the GALEX catalogs already had so few usable sources we did not mask the regions we did in our LBT mosaics around bright stars; therefore, so that the fields are of similar area, the  $N_{Hess}$  listed here are the values from our LBT catalogs before the bright star masks were applied.

## REFERENCES

- Adelman-McCarthy, J. et al. 2007, *ApJS*, 172, 634
- Alberets, S. et al. 2011, *ApJ*, 731, 28
- Bailin, J., Power, C., Norberg, P., Zaritsky, D., Gibson, B.K. 2008, *MNRAS*, 390, 1133
- Bakos, J., Trujillo, I., Pohlen, M. 2008, *ApJL*, 683,103
- Begeman, K.G. 1987, Kapteyn Institute, PhDT, 199
- Bertin, E., 2006, in *Astronomical Data Analysis Software and Systems XV*, ASP Conf. Series 351, 112
- Bertin, E., & Arnouts, S. 1996, *A&AS*, 117, 393
- Bland-Hawthorn, J., Vlajić, M., Freeman, K.C., Draine, B.T. 2005, *ApJ*, 629, 239
- Blanton, M.R. et al. 2003, *ApJ*, 592, 819
- Bush, S.J., Cox, T.J., Hernquist, L., Thilker, D., Younger, J.D. 2008, *ApJL*, 683, 13
- Buta, R. 1988, *ApJS*, 66, 233
- Cerviño, M., & Luridiana, V. 2004, *A&A*, 413, 145
- Chandar, Rupali; Fall, S. Michael; Whitmore, Bradley C. 2006, *ApJL*, 650, 111
- Christlein, D., Zaritsky, D. 2008, *ApJ*, 680, 1053
- Daigle, O., Carignan, C., Amram, P., Hernandez, O., Chemin, L., Balkowski, C., Kennicutt, R. 2006, *MNRAS*, 367, 469
- Dalcanton, J.J. et al. 2009, *ApJS*, 183, 67
- Davidge, T.J., Puzia, T.H., McConnachie, A.W. 2011, *ApJL*, 728, 23
- de Jong, R.S. et al. 2007, *IAUS*, 241, 503
- de Jong, R.S. et al. 2007, *ApJL*, 667, 49
- Fagiolini, M., Raimondo, G., Degl'Innocenti, S. 2007, *A&A*, 462, 107
- Fall, S.M., Chandar, R., & Whitmore, B.C. 2005, *ApJL*, 631, 133
- Ferguson, A.M.N., Wyse, R.F.G., Gallagher, J.S., Hunter, D.A. 1998, *ApJL*, 506, 19
- Fukugita, M., Shimasaku, K., Ichikawa, T. 1995, *PASP*, 107, 945
- Gehrels, N. 1986, *ApJ*, 303,336
- Giallongo, E., et al. 2008, *A&A*, 482, 349
- Gieles, M., Heggie, D.C., & Zhao, H. 2011, 413, 2509
- Gil de Paz, A. et al. 2005, *ApJL*, 627, 29
- Gil de Paz, A. et al. 2007, *ApJS*, 173, 185
- Godwin, J.G., Bucknell, M.J., Dixon, K.L., Green, M.R., Peach, J.V., Wallis, R.E. 1977, *Obs*, 97, 238
- Gogarten, S.M. et al. 2009, *ApJ*, 691, 115
- Graham, J.A. et al. 1997, *ApJ*, 477, 535
- Herbert-Fort, S. et al. 2009, *ApJ*, 700, 1977
- Herrmann, K.A., Ciardullo, R. 2009, *ApJ*, 705, 1686
- Hill, J. M., Green, R. F., & Slagle, J. H. 2006, *Proc. SPIE*, 6267, 62670Y
- Irwin, M.J., Ferguson, A.M.N., Ibata, R.A., Lewis, G.F., Tanvir, N.R. 2005, *ApJL*, 628, 105
- Jester, S. et al. 2005, *AJ*, 130, 873
- Karachentsev, I.D., Karachentseva, V.E., Huchtmeier, W.K., Makarov, D.I. 2004, *AJ*, 127, 2031
- Karachentsev, I.D. 2005, *AJ*, 129, 178
- Kazantzidis, S., Zentner, A.R., Kravtsov, A.V., Bullock, J.S., Debattista, V.P. 2009, *ApJ*, 700, 1896
- Kennicutt, R.C. 1989, *ApJ*, 344, 685
- Landolt, A. U. 1992, *AJ*, 104, 340
- Leitherer, C. et al. 1999, *ApJS*, 123, 3
- Leonard, D.C. et al. 2002, *AJ*, 124, 2490
- Makarova, L. 1999, *A&AS*, 139, 491
- Maloney, P. 1993, *ApJ*, 414, 41
- Martin, C.L., Kennicutt, R.C., Jr. 2001, *ApJ*, 555, 301
- Martin, D.C. et al. 2005, *ApJL*, 619, 1
- Monet, D.G. et al. 2003, *AJ*, 125, 984
- Nilson, P. 1973, *UGC*, C, 0000N
- Parker, R.J., Goodwin, S.P. 2007, *MNRAS*, 380, 1271
- Pohlen, M., Dettmar, R.-J., Lütticke, R., Aronica, G. 2002, *A&A*, 392, 807
- Pompei, E., & Natali, G. 1997, *A&AS*, 124, 129
- Ragazzoni, R. et al. 2006, *Proc. SPIE*, 6267, 33
- Rieke, G.H., Lebofsky, M.J. 1985, *ApJ*, 288, 618
- Roškar, R., Debattista, V.P., Stinson, G.S., Quinn, T.R., Kaufmann, T., Wadsley, J. 2008, *ApJL*, 675, 65
- Roškar, R., Debattista, V.P., Quinn, T.R., Stinson, G.S., Wadsley, J. 2008, *ApJL*, 684, 79
- Rownd, B.K., Dickey, J.M., Helou, G. 1994, *AJ*, 108, 1638
- Rubin, V.C., Peterson, C.J., Ford, W.K., Jr. 1975, *ApJ*, 199, 39
- Spitzer, L., Jr. 1958, *ApJ*, 127, 17
- Swartz, D.A., Yukita, M., Tennant, A.F., Soria, R., Ghosh, K.K. 2006, *ApJ*, 647, 1030
- Swaters, R.A., van Albada, T.S., van der Hulst, J.M., Sancisi, R. 2002, *A&A*, 390, 829
- Thilker, D.A. et al. 2005, *ApJL*, 619, 79
- Thilker, D.A. et al. 2007, *ApJS*, 173, 538
- Tonry, J.L., Dressler, A., Blakeslee, J.P., Ajhar, E.A., Fletcher, A.B., Luppino, G.A., Metzger, M.R., Moore, C.B. 2001 *ApJ*, 546, 681
- Trujillo, I., Martinez-Valpuesta, I., Martínez-Delgado, D., Peñarrubia, J., Gabany, R.J., Pohlen, M. 2009, *ApJ*, 704, 618
- Tully, B. 1988, *Nearby Galaxies Catalog* (Cambridge: Cambridge University Press)
- Vazquez, G., & Leitherer, C. 2005, *ApJ*, 621, 695
- Walter, F., Brinks, E., de Blok, W.J.G., Bigiel, F., Kennicutt, R.C., Thornley, M.D., Leroy, A. 2008, *AJ*, 136, 2563
- Weiner, B.J., Williams, T.B., van Gorkom, J.H., Sellwood, J.A. 2001, *ApJ*, 546, 916
- Werk, J.K. et al. 2010, *AJ*, 139, 279
- Werk, J.K., Putman, M.E., Meurer, G.R., & Santiago-Figueroa, N. 2011, *ApJ*, 2011, 735, 71
- Williams, B.F. et al. 2009, *AJ*, 137, 419
- Wolfe, A. M., Gawiser, E., Prochaska, J. X. 2005, *ARA&A*, 43, 861
- Wright, E.L. 2006, *PASP*, 118, 1711
- Zaritsky, D., & Christlein, D. 2007, *AJ*, 134, 135